Research Square

Preprints are preliminary reports that have not undergone peer review.
They should not be considered conclusive, used to inform clinical practice,
or referenced by the media as validated information.

Subducting Oceanic Fracture Zone Influences Slab Hydration, Seismicity, and Arc Magmatism in Ecuador

Cong Li

congli87@arizona.edu

University of Arizona https://orcid.org/0000-0002-4304-0235

Susan Beck

The University of Arizona

Colton Lynner

University of Delaware

Yi Wang

Innovation Academy for Precision Measurement Science and Technology, CAS

Anne Meltzer

Lehigh University

Mario Ruiz

Escuela Politecnica Nacional https://orcid.org/0000-0002-0872-6573

Article

Keywords:

Posted Date: November 20th, 2026

DOI: https://doi.org/10.21203/rs.3.rs-11710930/v1

License: This work is licensed under a Creative Commons Attribution 4.0 International License.
Read Full License

Additional Declarations: There is **NO** Competing Interest.

Subducting Oceanic Fracture Zone Influences Slab Hydration, Seismicity, and Arc Magmatism in Ecuador

Cong Li[1*], Susan L. Beck[1†], Colton Lynner[2†], Yi Wang[3†], Anne Meltzer[4†], Mario Ruiz[5†]

[1*]Department of Geosciences, University of Arizona, AZ, USA.

[2]Department of Earth Sciences, University of Delaware, Newark, DE, USA.

[3]State Key Laboratory of Precision Geodesy, Innovation Academy for Precision Measurement Science and Technology, Chinese Academy of Sciences, Wuhan, China.

[4] Department of Earth and Environmental Sciences, Lehigh University, Bethlehem, PA, USA,

[5]Instituto Geofísico at the Escuela Politécnica Nacional, Quito, Ecuador

*Corresponding author(s). E-mail(s): congli87@arizona.edu;

†These authors contributed equally to this work.

Abstract

Subducting oceanic fracture zones may influence slab dynamics, yet their subsurface structures and underlying mechanisms remain poorly constrained. Here we investigate subduction of the Grijalva Fracture Zone (GFZ) beneath Ecuador by constructing high-resolution three-dimensional shear-wave velocity model and analyzing intraslab seismicity. Our results reveal a transition from moderately-dipping northern Nazca slab to a shallowly-diping southern slab across the inferred landward continuation of the GFZ. A slab low-velocity corridor is observed at ~75-110 km depth along the GFZ continuation, consistent with a hydrated fracture zone. Intermediate-depth earthquakes cluster near the corridor and exhibit predominantly downdip-extensional faulting, with nodal planes transverse to the inferred GFZ. Within the overriding plate, low-velocity anomalies occur in the mantle wedge and upper-to-middle crust beneath the northern arc but are localized in the lower crust farther south. We propose that the dehydration and mechanical weakness along the GFZ facilitate fluid release and localize intraslab earthquakes, without requiring fracture-zone-parallel fault reactivation or a slab tearing. The along-strike contrasting low-velocity structures may reflect different magmatism due to various slab geometry and mantle-wedge conditions, with localized contributions from GFZ-derived fluids. These findings provide new insights on how inherited fracture zones can influence the slab deformation, intermediate-depth seismicity, and arc magmatism.

Introduction

Inherited structural heterogeneities in oceanic lithosphere can profoundly influence the dynamics of subduction zones. Oceanic fracture zones, the inactive extensions of transform faults that offset

mid-ocean ridge segments, represent long-lived lithospheric heterogeneities characterized by contrasts in age, thermal structure, and mechanical properties[1]. Faulting along oceanic fracture zones may facilitate seawater infiltration and mantle hydration prior to subduction, introducing localized reservoirs of structurally bound water into the oceanic lithosphere [2,3]. During subsequent subduction, progressive breakdown of these hydrous minerals release fluids that may contribute to intermediate-depth intraslab seismicity and influence magmatic processes within the overlying plate[4-7]. Numerical models further suggest that inherited mechanical weaknesses associated with fracture zones can promote localized slab deformation and potentially cause slab tearing[8-11]. Despite these proposed hydrological and mechanical effects, the extent to which fracture-zone-related heterogeneities can persist at depths and how they influence slab deformation, intraslab seismicity, and arc magmatism remains poorly constrained.

The Grijalva Fracture Zone (GFZ), located within the Nazca Plate offshore of southern Ecuador in South America, provides a natural laboratory for investigating these processes (Fig. 1). The GFZ developed during fragmentation of the Farallon Plate in the early Miocene[12]. North of the GFZ, oceanic lithosphere was generated at the Cocos-Nazca spreading center and subsequently modified by the Galápagos hotspot, which formed the Carnegie Ridge and is currently subducting beneath the northern Ecuador[13,14]. South of the GFZ, the incoming plate consists of older Nazca lithosphere inherited from the Farallon Plate[15,16]. The lithosphere north and south of the GFZ has ages of ~9-22 Ma and ~30-35 Ma, respectively, with an age offset of ~8-10 Myr across the boundary near the trench[14] (Fig. 1a). The GFZ is also marked by a pronounced bathymetric step, with the seafloor deepening southward by ~500 m over a horizontal distance of 25-30 km[17].

The GFZ is currently subducting obliquely beneath the Ecuadorian margin, where the Nazca Plate converges with South America at ~56-60 mm/yr along an azimuth of ~83°[18]. The overridng plate comprises a forearc region underlain by accreted mafic oceanic plateaus and island arcs and a continental Cordillera region belonging to the South American Plate[19] (Fig. 1b). The subsurface trajectory of the GFZ is largely uncertain, although previous studies have proposed that its landward continuation extends beneath the Ecuadorian volcanic arc[20-22] (Fig. 1a). Here, we define the possible GFZ continuation zone bounded by projections of the offshore fracture-zone strike and the plate convergence direction (Fig. 1a).

The influnce of the subducted GFZ on the Ecuadorian subduction system also remains a subject of debate. The global model suggests significant along-strike variations in slab geometry beneath Ecuador, with a relatively steeply dipping slab to the north and a shallower slab to the south[23] (Fig. 1b). However, the scarcity of intermediate-depth earthquakes leave the regional-scale slab geometry poorly constrained, especially across the projected GFZ continuation. A cluster of intermediate-depth earthquakes at ~150-250 km depth near the GFZ continuation has been interpreted as evidence for either three-dimensional slab contortion[22] or slab tearing[24]. Whether these deep structural variations extend to shallower depths and whether they relate to inherited GFZ heterogeneity remain unclear. In addition, Quaternary volcanism in Ecuador exhibits pronounced along-strike segmentation across the GFZ continuation zone, with a gap near 0.8-1.1°S

separating northern and southern volcanic segments[21,25] (Fig. 1c). However, the magmatic structures beneath the volcanic arc and their possible interaction with the subducted GFZ are unresolved. Resolving these questions requires improved constraints on the geometry and internal structure of the slab and their relationship to seismicity and the overlying volcanic arc.

Recent deployments of dense broadband and nodal seismic arrays, together with long-term permanent seismic stations, have substantially improved seismic data coverage across the Ecuadorian margin (Fig. 1b), providing an opportunity to investigate structures of both the subducting slab and overriding plate. In this study, we present a high-resolution three-dimensional shear-wave velocity (Vs) model of the crust and upper mantle beneath Ecuador, constructed through a trans-dimensional Bayesian joint inversion of Rayleigh-wave phase-velocity dispersion curves and teleseismic receiver functions (see *Methods* for detailed description of tomographic model construction). The resulting model constrains shear-wave velocity variations and major velocity discontinuities at depths of 5-110 km. We identify pronounced along-strike variations in slab geometry across the projected GFZ continuation, a localized slab low-velocity zone associated with the inferred GFZ, and distinct low-velocity anomalies within the overriding crust and mantle wedge beneath the volcanic arc. By integrating these observations with earthquake distributions and focal mechanisms, petrophyscial modeling, and volcanic geochemistry, we provide new evidence on the persistence of inherited fracture-zone heterogeneity and its influence on slab deformation, intraslab seismicity, and arc magmatism.

Results

Shear-velocity Structures of the Ecuadorian Lithosphere

Our tomographic model reveals significantly lateral contrasts in crustal structures between the forearc and the Cordillera regions of the Ecuadorian margin (Figs. 2 and 3). The forearc is characterized by Vs values of ~3.6-3.9 km/s at depths of 10-25 km, increasing rapidly to values exceeding 4.0 km/s at greater depths (Figs. 2a, 2b and 3). In contrast, the Cordillera reveals more heterogenous velocities of ~3.2-3.8 km/s above 45 km depth, followed by an abrupt increase to 4.0-4.2 km/s across depths of 45-55 km (Figs. 2b and 3). The sharp velocity discontinuity associated with the crust-mantle boundary deepens systematically from the forearc toward the Cordillera, leading to a lateral Vs decrease across the forearc-Cordillera boundary in map view at a depths of ~25-45 km (Figs. 2a and 2b).

Below the crust, prominent higher-than-surrounding velocity bands (Vs=4.4-4.7 km/s) are imaged beneath the northern and southern Ecuador and exhibit landward-dipping geometries (Figs. 2c, 2d and 3). We delineate the upper boundaries of these high-velocity bands by identifying the locations of maximum positive Vs-perturbation gradients at depths greater than 50 km. The resulting boundaries are broadly consistent with subduction-zone seismicity distribution and exhibit pronounced along-strike variations in dip angle and landward extent (Figs. 3, S12, S13). In northern Ecuador, the high-velocity anomaly extends from depths of ~50-60 km beneath the coastal forearc to ~80-100 km beneath the western Cordillera, with the delineated upper boundary

dipping at ~20-25° (Cross-sections AA' and BB' in Fig. 3, Fig. S13). In contrast, the velocity high in southern Ecuador extends farther inland beneath the central Cordillera over a comparable depth range, with a shallower dip of ~12-15° (Cross-sections CC' and DD' in Fig. 3; Figure S13). Between the high-velocity domains, a relatively lower-velocity zone (SLVZ), characterized by Vs values of 4.2-4.35 km/s, is observed at depths of 75-110 km between 1°S and 3°S (Figs. 2c and 4a; Cross-sections EE' in Fig. 5). This anomaly contrasts with the surrounding high-velocity regions, spans ~80-150 km laterally, and spatially overlaps the projected landward continuation of the GFZ.

Three major lower-than-surrounding velocity anomalies are imaged within the overridng plate beneath the Ecuadorian volcanic arc. The first (CLVZ1) is located within the northern volcanic arc crust at depths of ~15-30 km and has Vs values of 3.2-3.4 km/s (Fig 2a., Cross-section AA' in Fig. 3). The second (CLVZ2) occurs within the southern volcanic arc crust at depths of ~40-55 km, with Vs values of 3.5-3.7 km/s over a lateral extent of ~100 km (Fig 2b, Cross-section BB' in Fig. 3). The third (MLVZ), characterized by Vs values of 4.0-4.2 km/s, extends through the uppermost mantle at depths of ~60-100 km. This anomaly distributes beneath much of the volcanic arc at depths of ~55-65 km but becomes restricted to the northern arc below ~70 km depth (Fig. 2c and 2d, Cross-section AA' and BB' in Fig. 3). A series of uncertainty and resolution analyses demonstrate that the major observed features described above are robustly resolved in our tomographic model (see *Methods* for detailed description of model uncertainty analysis and resolution test).

Subduction-zone Earthquake Distribution and Focal Mechanisms

Our compiled earthquake catalog[26-29] reveals pronounced spatial variations in subduction-zone seismicity and associated focal mechanisms across Ecuador. Earthquakes shallower than 50 km are concentrated along the coastal region of northern and southern Ecuador and are characterized predominantly by reverse-faulting mechanisms (Figs. 1a, 4b, 4c, and S18c). In contrast, relatively few earthquakes occur within the projected GFZ continuation zone at these depths, where strike-slip mechanisms are more prevalent (Fig. 4c).

At depths greater than 50 km, intraslab earthquakes extend to ~100 km beneath northern Ecuador and to ~250 km within the projected GFZ continuation zone and beneath southern Ecuador, revealing a along-strike contrast in the depth extent of the Wadati-Benioff zone (Figs. 4b). Three earthquake clusters are identified near the projected GFZ continuation (Fig. 4b), accounting for ~80% of the intraslab earthquakes (Figs. 4c and S18d). Cluster 1 lies immediately north of the inferred northern boundary of the projected GFZ continuation zone at depths of 50-110 km, whereas Clusters 2 and 3 occur within the projected zone at depths of 50-130 km and 150-250 km, respectively. Normal-faulting mechanisms predominate among the deep intraslab earthquakes (Figs. 4c and S18a). After correction for local slab geometry, the T axes of the normal-faulting earthquakes within the projected GFZ continuation zone are oriented approximately parallel to the local slab-dip direction, while the nodal planes are oriented perpendicular or oblique to the GFZ

strike (Figs. 4d, and S19). In comparison, normal-faulting earthquakes outside the GFZ zone exhibit similar T-axis and nodal-plane orientations, despite substantially fewer events (Figs. 4e)

Discussion

Subducting Slab Geometry beneath the Ecuadorian Margin

The geometry of the subducting Nazca lithosphere beneath Ecuador has long been debated, particularly in the northern area where intermediate-depth seismicity is sparse (Figs 1a and 4b). Subduction of the buoyant Carnegie Ridge has been proposed to induce local-scale slab flattening beneath northern Ecuador, explaining the scarcity of deep earthquakes[30]. Alternatively, the limited depth extent of intermediate-depth seismicity may reflect the warmer thermal state of the younger subducting lithosphere without requiring slab flatterning[22]. Our tomographic model provides independent constraints on the slab geometry beneath Ecuador. The upper boundaries of the landward-dipping high-velocity anomalies are spatially consistent with the distribution of intraslab seismicity and the previously published slab interface models[23,31] (Figs. 3 and S13). The observed Vs values within the anomalies are also broadly consistent with those predicted for dry harzburgite along the slab pressure-temperature trajectory beneath Ecuador (Fig. S20), further supporting their interpretation as the subducting oceanic lithosphere. Moreover, the imaged slab reveals a moderately dip angle (~20-25°) beneath northern Ecuador, compared with a shallower dip (~12-15°) to the south (Fig. 3).

The moderately dipping slab beneath northern Ecuador argues against the previously proposed flat-slab configuration[30] within the resolved depth range but supports relatively steep geometry inferred by ref.[22] Previous geochronology studies suggest that Carnegie Ridge subduction began relatively recently[32-34], while recent seismic studies indicate that its inland extension is largely confined to the coastal forearc[26,35]. Together, these observations suggest that the Carnegie Ridge subduction beneath northern Ecuador has not significantly changed the slab geometry, and the imaged moderately dipping slab likely represents oceanic lithosphere that entered the trench before the ridge's arrival.

In south Ecuador, the imaged shallow-dip slab is consistent with the regional extension of Peruvian flat-slab system, which has been suggested to be associated with the subduction of buoyant oceanic plateau south of our study region [36]. Notably, the moderate-to-shallow slab dip transition between northern and southern Ecuador coincides with the projected landward continuation of the GFZ (Fig. S13). This spatial correspondence suggests a slab zone along the GFZ accommodating the differential geometries of the adjacent slab segments.

Nature of the Low-Velocity Slab Zone

A distinct low-velocity zone (SLVZ) is imaged within the subducting slab, whose spatial distribution is consistent with the projected GFZ continuation zone (Figs. 2c, d and 4a; Cross-section E-E' in Fig. 5). The anomaly extends from ~75 to 110 km depth, with a lateral width of ~80 km defined by the 4.30 km/s contour and ~150 km defined by the 4.35 km/s contour. Relative

to the adjacent high-velocity slab domains with average Vs of 4.5 km/s, the SLVZ exhibits a significant velocity reduction of 0.15-0.30 km/s (3.3-6.7%). This contrast exceeds the maximum model uncertainty of 0.05 km/s (Fig. S12), and the resolution tests with comparable dimensions of the SLVZ demonstrate its imaging robustness (Figs. S14-S17),

The observed velocity reduction within the SLVZ is unlikely to be explained solely by thermal effects or seismic anisotropy. Our petrophysical modeling for dry oceanic mantle rocks indicate that pressure-temperature increase along representative slab-mantle thermal trajectories beneath Ecuador produce Vs reductions of less than 0.1 km/s, substantially smaller than the observed velocity low (Fig. S20). Although numerical simulations[5] suggest that subduction of a hydrated fracture zone may locally increase temperatures near the slab top by ~100°C, such warming is expected to produce only modest additional reductions. Partial melting within slab could further reduce velocity but would require temperatures to exceed the hydrous solidus of ultramafic rocks. Typical temperatures of a hydrous solidus at the relevant pressures (800-900°C or higher[37,38]) are approximately 300-400 °C higher than those predicted along the Ecuadorian slab trajectories (Fig. S20), making partial melting hypothesis less likely without an additional heating mechanism. In addition, seismic anisotropy associated with inherited oceanic fabrics or slab deformation may also influence isotropic velocity estimates. Rayleigh-wave studies have reported that oceanic lithosphere has typical peak-to-peak azimuthal anisotropy of ~3-4% in the central Pacific Ocean[39] and less than ~2% in the Alaska and Cascadia subduction zones[40,41]. Other studies have identified shear-wave radial anisotropy of ~1-3% in the oceanic uppermost mantle[42,43]. Assuming a reference velocity of 4.5 km/s, these anisotropy magnitudes correspond to maximum velocity deviations of ~1.5-2% (0.07-0.09 km/s) for azimuthal anisotropy and ~0.5-1.5% (0.02-0.07 km/s) for radial anisotropy, which cannot fully account for the observed SLVZ.

The close spatial correlation between the SLVZ and the projected GFZ continuation suggests that this inherited lithospheric structure may contribute to the observed low-velocity slab domain. Faulting associated with fracture zones can facilitate seawater infiltration into the oceanic mantle before subduction, promoting serpentinization and introducing compositional heterogeneous domains within mantle lithosphere[4,5,7]. Seismic observations at the Middle America trench reveal deep bending-related faults penetrating the oceanic crust and extending ~20 km deep into the upper mantle, which facilitate local mantle hydration[44-46]. Numerical models further suggest that serpentinized fracture zones can enhance water transport and fluid release during subduction[5]. If the GFZ introduced an elevated water inventory into the Nazca lithosphere, hydrous mantle assemblages could persist to intermediate depths and cause localized velocity variations.

To evaluate this hypothesis, we calculated the Vs values for hydrated mineral assemblage endmembers along the slab thermal trajectories in the Ecuadorian subduction zone (Fig. 6a). The calculations indicate that the observed SLVZ velocities are larger than predicted Vs of antigorite-rich serpentinite (90 vol.% antigorite) but lower than those for serpentine dunite (40 vol.% antigorite), suggesting that mixtures of hydrated and relatively dry mantle rocks can reproduce the observed velocity low (Fig. 6b). The modeled stability intervals of these hydrous mineral

assemblages also overlap with the imaged depth range of the SLVZ (Fig. 6b). We further estimate an antigorite content of ~20-37 vol.% corresponding to the observed SLVZ within the subducting slab (Fig. 6c), which is roughly consistent with laboratory measurement results for typical serpentinized mantle rocks[47,48]. The agreement between the tomographic imaging and petrophysical modeling thus supports the interpretation of the SLVZ as a hydrated slab-mantle domain likely associated with the GFZ.

GFZ-related Slab Deformation and Intraslab Earthquakes

Integration of the imaged low-velocity slab zone (SLVZ) with intraslab seismicity and earthquake focal mechanisms provides insights into the possible role of the GFZ in slab deformation. Intraslab earthquakes are strongly concentrated within the projected GFZ zone (Fig. 4b), with two prominent clusters (Clusters 1 and 2) located near the lateral margins of the SLVZ at depths of ~50-130 km (Figs. 4b, 5a and 5b). The predominance of normal-faulting mechanisms with downdip-oriented T axes among these earthquakes indicates a primarily downdip-extensional regime within the subducting slab (Fig. 4c). However, similar focal mechanisms and T-axis orientations observed inside and outside the projected GFZ continuation suggest that this extensional regime is regionally pervasive rather than confined to the GFZ (Fig. 4d and 4e). After correction for local slab dip, the nodal planes of the intraslab earthquakes are predominantly oriented transverse to the GFZ strike (Figs. 4d and 4e). Together, these observations suggest that the GFZ preferentially localize intraslab faulting under a shared downdip-extensional regime, rather than producing a distinct stress field and reactivating GFZ-parallel faults.

The concentration of seismicity near the inferred hydrated GFZ corridor may reflect dehydration reactions, deformation accommodation or a combination of both. Experimental studies have demonstrated that dehydration of antigorite-bearing rocks can trigger faulting through dehydration embrittlement and/or stress transfer to adjacent load-bearing minerals[49,51]. Our petrophysical modeling predicts a transition from highly hydrated to moderately hydrated minerals at ~75-95 km depth along slab thermal trajectories near the oceanic Moho, followed by a transition to less hydrated minerals at ~95-120 km along deeper trajectories (Fig. 6a and 6b). These predicted hydrous-mineral transition depths overlap peaks in the earthquake depth distributions within the corresponding slab domains (Fig. 7), supporting that progressive dehydration of water-riched GFZ contributes to intraslab earthquake nucleation[49-51]. In addition, inherited fault structures and hydrated heterogeneity within the GFZ corridor may also introduce mechanical weakening relative to surrounding mantle. In this context, the hydrated GFZ corridor may preferentially localize the slab deformation, while mechanical contrasts with the surrounding slab could further promote faulting. Although the relative contributions of dehydration and deformation accommodation are uncertain, their combined effects provide a plausible explanation for the observed concentration of intraslab seismicity near the subducting GFZ.

A previous earthquake hypocenter study[24] proposed possible slab tearing along the GFZ at depths of ~150-250 km, which is likely driven by differential deformation between adjacent slab segments

and contributes to the El Puyo earthquake cluster (Cluster 3 in Fig. 4b). Recent seismic body-wave tomography[52] has provided further support for this hypothesis and suggest the tearing may faciliate asthenospheric upwelling and contribute to back-arc magmatism. Our model cannot evalue the proposed deep slab tearing due to its limited imaging depth. Nevertheless, the tomographic results reveal no clear through-going interruption of the subducting slab at depths shallower than 110 km. The observed nodal-plane orientations provide little evidence for hypothesis of preferential GFZ-parallel faults reactivation that has been interpreted as principal mechanism for slab tearing[24]. Instead, our observations favor a structurally coherent but mechanically heterogeneous, hydrated corridor at the resolved depths rather than development of a mature slab tear. A possible senario is that the hydrated fracture zone imaged at shallow depths progressively influence slab deformation during its continued subduction, contributing to deep slab contortion[22] or even tearing[24].

Interaction between GFZ-associated Slab Geometry Variations and Arc Magmatism

Our tomographic model reveals three distinct low-velocity anomalies within the overriding plate, suggesting varied magmatic structures along the Ecuadorian volcanic arc. Beneath the northern arc, CLVZ1 occurs in the upper to middle crust and has Vs of ~8-13% lower than the reference value (3.7 km/s) for typical felsic crustal rocks (Figs. 8a and 9a). In contrast, CLVZ2 is located in the lower crust beneath the southern arc, with a Vs reduction of ~5-10% compared to reference mafic crustal rocks (3.9 km/s; Figs. 8a and 9b). The upper-mantle anomaly, MLVZ, mainly distributes beneath the northern arc and exhibits a Vs of ~4.5-9% lower than the representative mantle rock velocity (4.4 km/s; Figs. 8a and 9c). The petrophysical calculations using bulk compositions of representative crustal and mantle rocks in Ecuadorian Cordillera indicate that the observed velocities in these anomalies are substantially lower than predictions for melt-free mineral assemblages at their respective solidus temperatures, indicating that elevated temperatures alone are insufficient to explain these anomalies and that partial melts may be present. Using the melt-velocity relationships derived from effective medium models[53,54], we estimate the melting fraction range of ~4.5-12% for CLVZ1, ~2.7-8% for CLVZ2, and ~2.5-7.5% for MLVZ (Figs. 8b-8d, S21). These observations and analyses suggest magma accumulation at different crustal and upper-mantle depths beneath the northern and southern arcs.

The imaged contrasting magmatic structures along the Ecuadorian arc spatially coincide with the changes in slab geometry across the inferred GFZ continuation. The slab dips more steeply beneath the northern arc but becomes progressively shallower toward the south, whereas the continental Moho remains at a relatively uniform depth of 50-55 km (Fig. S22). These architectures thus lead to a southward decrease in mantle wedge thickness (Fig. 9d), potentially influencing mantle circulation, thermal conditions, and spatial distribution of partial melting[55-57]. The thicker mantle wedge beneath the northern arc likely facilitates asthenosphere circulation, promotes upper mantle melting and favors subsequent crustal magmatism, which is consistent with the observation of widespread MLVZ and CLVZ1 (Fig. 9a and 9c, Cross-sections AA' and BB' in Fig. 3). In contrast, the southward transition to a thinner mantle wedge across the GFZ restricts asthenosphere circulation and available volume of mantle for melting, leading to the more limited observation of

MLVZ beneath the southern arc (Fig 9b, Cross-section CC' in Fig. 3). Farther south, the shallowly dipping slab extends beneath much of the Cordillera, further reducing mantle-wedge thickness and suppressing mantle melting. This is consistent with disappearance of observed low-velocity anomalies and termination of Quaternary volcanism in southern Ecuador (Fig. 5c; Cross-section DD' in Fig. 3).

Contrasting oceanic lithospheric properties across the GFZ can also influence on arc magmatism by modifying slab thermal condition and fluid release. Previous geochemical studies[20,58] reported a southward decrease in Ba/Th ratios of frontal-arc volcanic rocks (Fig. 9e), which are interpreted to reflect a reduced contribution from slab-derived aqueous fluids toward the southern arc. In this scenario, the younger and warmer oceanic lithosphere north of the GFZ may promote dehydration at shallower depths, enhancing fluid transfer into the mantle wedge and facilitating flux melting. In contrast, the relatively older and colder lithosphere to the south may retain hydrous minerals to greater depths, shifting fluid release farther downdip and potentially reducing fluid input beneath the volcanic front. These thermal and compositional contrasts may therefore contribute to the observed along-strike variations in mantle melting and arc magmatism.

Dehydration process associated with subducting oceanic fracture zone may provide additional source of slab-derived fluids into mantle wedge and improve arc magmatism[5]. The imaged slab low-velocity domain (SLVZ) in our model is consistent with a hydrated GFZ corridor that can release fluids at intermediate depths during progressive metamorphic dehydration. The spatial correlation between SLVZ and the lower-crustal CLVZ2 supports that GFZ-related fluid release likely contribute to mantle melting and subsequent magma accumulation beneath the southern arc (Fig. 9b and 9c). The hypothesis is also consistent with localized enrichments in fluid-mobile elements and anomalous chlorine concentrations in primitive melt inclusions from some southern Ecuadorian volcanic rocks[58]. However, these localized geochemical signatures are less pronounced compared to the broader along-arc variations associated with slab geometry and thermal structural changes (Fig. 9e), implying the GFZ-related dehydration may exert a localized rather than regional influence on arc magmatism.

Integrated Tectonic Model and Broad Implications

Together, our tomographic and earthquake observations provide an integrated view of how the subducted GFZ may influence slab deformation, intermediate-depth seismicity, and arc magmatism beneath Ecuador (Fig. 10). We propose that the GFZ represents an inherited lithospheric boundary separating the younger, moderate-dipping Nazca lithosphere to the north from the older, shallower-dipping lithosphere to the south. Inherited fault structures and lithospheric heterogeneity along the GFZ can form a mechanically weak corridor that accommodates deformation between the contrasting slab segments under a prevailing downdip-extensional stress regime. Enhanced hydration and serpentinization within this corridor can persist to depths of ~75-110 km, where progressive breakdown of hydrous minerals release fluids and contribute to the concentration of intermediate-depth earthquakes. The GFZ-associated slab

geometry variations and hydration can also influence arc magmatism. Beneath the northern arc, the steeper slab and thicker mantle wedge facilitate hot asthenospheric circulation and promote more extensive mantle melting and the development of upper-to-middle-crustal magmatic structures. In contrast, progressive slab shallowing toward southern Ecuador restricts the extent of mantle melting. Localized fluid release from the hydrated GFZ corridor could additionally contribute to mantle melting and lower-crustal magma accumulation along the inferred GFZ continuation, but it is superimposed on the broader magmatic variations associated with slab geometry and thermal conditions (Fig. 10).

The influence of inherited oceanic structures on subduction dynamics is increasingly recognized across different convergent margins. Along the Valdivia Fracture Zone in southern Chile, for example, localized intermediate-depth seismicity and seismic low-velocity anomalies have been interpreted as evidence for fracture-zone reactivation and enhanced fluid release[59,60]. Similar reactivation of oceanic faults and fracture zones and associated fluid circulation and arc magmatism has been recognized in other subduction zone such as the Middle America[45,61] and Lesser Antilles[62]. In some setting, the inherited oceanic lithosphere weaknesses may facilitate slab tearing[63]. However, our observations indicate that the GFZ can localize intraslab deformation and enhance fluid release without requiring reactivation of faults parallel to the inherited fracture zone or the development of a mature slab tear. This suggests that subducting oceanic fracture zone may preferentially localize deformation under the regional stress field rather than creating a distinct local stress field. In this case, dehydration reaction within the fracture zone may still help develop faults, but orientations of fault planes depend on dominant stress tensor and frictional properties. Moreover, our results indicate that an inherited oceanic fracture zone can coincide with a transition in slab geometry and overriding-plate magmatic structures. Numerical studies[5] have shown that fracture-zone hydration can enhance fluid release and mantle melting, consistent with prominent geochemical anomalies of arc magmas in some subduction zones. Our observations extend this framework by suggesting that the magmatic expression of a hydrated fracture zone may depend on its interaction with broader variations in slab geometry, mantle-wedge structures, and thermal conditions. These findings provide new insights into how inherited oceanic lithospheric heterogeneities can persist during subduction and how they interact with slab deformation and arc magmatism.

Materials and Methods

Rayleigh-wave Dispersion Curves Extraction and Phase-velocity Map Inversion

We use continuous seismic waveforms from 166 three-component broadband stations across the Ecuadorian forearc and volcanic arc (Fig. 1b). The dataset includes records from a permanent network[64] (EC; 2016-2024) and three temporary networks[65-67] (8G, 2016-2017; XE, 2016-2017; XF, 2021-2022). Rayleigh waves were extracted from both ambient noise and teleseismic events. For ambient noise, we computed empirical Green's functions by cross-correlating daily vertical-component waveforms between station pairs, following the procedure from ref.[68]. For teleseismic

records, we selected 2128 earthquakes with epicentral distance of 20°-120° and moment magnitudes ≥ 5.5 (Fig. S1). Clear Rayleigh-wave signals are observed at periods of 8-30 s in ambient noise cross-correlations and at periods of 20-80 s in teleseismic records (Figs. S2 and S3). Phase-velocity dispersion curves were measured from the extracted Rayleigh-wave signals using automated frequency-time analysis method[69]. We retained high-quality measurements with signal-to-noise ratio greater than 5 for ambient noise and greater than 10 for teleseismic earthquake data. The final dataset includes 2332 ambient-noise dispersion measurements and 26279 teleseismic dispersion measurements (Fig. S4).

Interstation dispersion measurements were inverted to obtain phase-velocity maps at multiple periods, with a grid spacing of $0.1^{\circ} \times 0.1^{\circ}$. For the short-period ambient noise data, we independently inverted the dispersion measurements using both Eikonal tomography[70] and ray-theoretical tomography[71]. The two methods yield consistent first-order phase velocity-patterns across the study region (Figs. S5-S7). We used the average of the resulting phase-velocity maps in subsequent analyses. For long-period teleseismic earthquake data, phase velocities were inverted using the Helmholtz tomography[72]. The resulting phase-velocity maps agree well with those from the ambient-noise inversion over the overlapping period range of 20-30 s (Figs. S6b and S7). Finally, we combined the short- and long-period phase-velocity maps to generate a continuous dataset spanning periods of 8-80 s (Fig. S8), providing sensitivity to crustal and upper mantle structures at depths of ~5-110 km.

Teleseismic Receiver Functions

We compiled 18477 high-quality teleseismic P-wave receiver functions (RFs) from ref.[36,73,74], which were calculated from recordings of the broadband seismic networks described above together with an additional 409 nodal stations deployed across the Ecuadorian margin (Fig.1a). RFs were filtered with a Gaussian function with a width of 2.5, corresponding to high-frequency cutoffs of ~1.25 Hz. We removed moveout effects of RFs using a reference slowness of 0.06 s/km. We then grouped the RFs within a 5-km radius around each station and extracted their azimuthally independent component using the harmonic stripping method[75]. The resulting stacked RFs and their associated uncertainties were used in the subsequent joint inversion (Fig. S9).

Joint Inversion of Rayleigh-wave Dispersion Curves and Receiver Functions

We obtained depth-dependent shear-wave velocity (Vs) profiles at each inversion grid point by jointly inverting Rayleigh-wave phase-velocity dispersion curves and RFs using a trans-dimensional Bayesian-Markov chain-Monte Carlo framework[76,77]. Velocity profiles are parameterized using a set of velocity-depth pairs (i.e. Voronoi cells). A velocity discontinuity is introduced when the velocity difference between adjacent Voronoi cells exceeded 0.1 km/s over a vertical separation of ≤10 km, with the interface placed midway between the two cells. Elsewhere, the velocity structure was represented by a cubic (third-degree) B-spline when fewer than three cells were present and a quartic (fourth-degree) B-spline otherwise. This hybrid parameterization

preserves sharp velocity contrasts while allowing smooth variations where discontinuities are not required by the data[75] (Fig. S10).

The prior searching range for Vs, depth and the number of Voronoi cells were set as 2-5 km/s,0-100 km and 0-20, respectively. Data noise level was allowed to vary from zero to the maximum uncertainties that were esitimated from the Eikonal and Helmholtz tomography for dispersion cruves and from harmonic-stripping analysis for RFs (Fig. S9). To account for the decreasing RF constraint away from seismic stations, the relative weights of the dispersion and RF datasets varied with the distance to the nearest station. At station locations, dispersion curves and RFs were assigned weights of 0.3 and 0.7, respectively. These weights gradually changed to 1.0 and 0.0 at distances $\geq$150 km. The Vp/Vs ratio between velocity discontinuities was also allowed to vary between 1.70 and 1.95, although it is primarily constrained by shallow discontinuities that generate strong RF multiples[77].

At each grid point, we performed the inversion using 20 independent Markov chains with 20,000 iterations per chain. We excluded chains whose misfits exceeded the overall minimum misfit value by more than 5%. We then randomly selected 3,000 models from the remaining well-converged chains and calculated their ensemble average to obtain the final one-dimensional Vs profile at each grid point (Fig. S10). The resulting one-dimensional profiles were interpolated onto a three-dimensional velocity model with a horizontal spacing of 5 km.

Model Uncertainty and Imaging Resolution

We evaluated uncertainties in our final model by considering contributions from both the phase-velocity map construction and the subsequent joint inversion. Uncertainties in the phase-velocity maps were estimated from the standard deviation of the mean slowness measurements obtained from Eikonal and Helmholtz tomography. For short-period (8-30 s) phase-velocity maps, uncertainties are generally $<$0.05 km/s but locally increase to ~0.08-0.10 km/s near the Gulf of Guayaquil (~2^{o}S), where station coverage is relatively sparse (Fig. S11a). For long-period (20-80 s) maps, uncertainties are $<$0.03 km/s across most of the study region (Fig. S11b). We further assessed the influence of station distribution by comparing phase-velocity maps obtained from Eikonal and ray-theoretical tomography (Figs. S6 and S7). Despite their different sensitivities to station coverage, both methods recover similar first-order phase-velocity structures across most of the study area, with average differences of $<$0.05 km/s (Figs. S5-S7). Larger differences are restricted primarily to the northernmost study region and the Gulf of Guayaquil, where station coverage is limited. For joint inversion, we calculate the uncertainty in each Vs profile using the standard deviation of the posterior Vs distribution at every depth (Figs. S12). Posterior uncertainties are generally $<$0.05 km/s throughout most of the crust and upper mantle but locally increase to ~0.10-0.12 km/s near first-order velocity discontinuities.

We conducted a series of recovery tests to evaluate the spatial resolution of the final tomographic velocity model (Figs. S14-S17). Tests using short-period (8-30 s) ambient-noise dispersion data primarily assess structures at depths of ~5-30 km, whereas those using long-period (20-80 s)

teleseismic dispersion data assess structures at depths of ~20-120 km. Our tests demonstrate that the ambient-noise data can well recover anomalies with spatial scale ≥ 0.75°×0.75° beneath the northern and central Ecuador, where station coverage is relatively dense (Figure S14). The minimum resolvable spatial scale increases to ~1.0°×1.0° toward southern Ecuador, where station coverage is sparser (Figure S15). In comparison, teleseismic dispersion data at periods of 20-80 s reliably recover anomalies with scale ≥ 0.75°×0.75° across most of the study region (Figs. S16 and S17).

Overall, our analyses indicate that the final Vs model is generally constrained to within ~0.05 km/s across most of the study region, with larger uncertainties of ~0.10-0.12 km/s occurring locally in areas of sparse station coverage and near major velocity discontinuities. Further resolution tests demonstrate that the major observed features in this study can be robustly resolved.

Seismicity and Earthquake Focal Mechanism

We compiled earthquake catalogs for events with magnitudes ≥ 2.0 during 2010-2022 from recent seismic studies[26,27,29]. These catalogs substantially improve the earthquake identification and accuracy of hypocenter locations by incorporating data from recently deployed seismic arrays. We identified and removed duplicate events among the catalogs if events occurring within 10 s and with hypocentral separations <10 km. We also excluded aftershocks occurring within one year of the 2016 Pedernales earthquake to better characterize the background seismicity.

We compiled focal mechanisms for earthquakes with magnitudes ≥ 3.8 between 2009 and 2025 from the Ecuadorian national earthquake catalog (IG-EPN) and ref.[28], retaining only well-constrained focal mechanisms based on the quality assessments provided by the original catalogs. See ref.[28] for detailed information on the construction of the earthquake catalogs and related quality assessment. We identified subduction-zone earthquakes as events located within the slab or ≤5 km above the slab interface defined by ref.[30], supplemented by the Slab2 model[23] where the model from ref.[30] is unavailable. For each focal mechanism, we calculated the P, T, and B axes and classified the faulting style based on their plunge angles using the FMC software[78] (Figs. 4c). The P, T, and B axes of subduction-zone earthquakes were then rotated into a slab-relative coordinate system using the local slab strike and dip derived from the published slab models, allowing us to evaluate deformation relative to the local slab geometry (Figs. 4d and 4e, S19a and 19b). To further examine the relationship between fault orientations and the GFZ strike, we additionally corrected the nodal-plane orientations for local slab dip by rotating them about a horizontal axis parallel to the local slab strike (Fig S19c and 19d).

Petrophysical Modeling of Hydration in the Subducting Slab and Partial Melting in the Overriding Plate

We performed petrophysical modeling to investigate the physical origins of the low shear-wave velocity (Vs) anomalies identified in our tomographic model. We first assessed the potential contribution of slab-mantle hydration to the observed velocity reductions. Isotropic Vs was

calculated for representative dry and hydrated harzburgitic mineral assemblages from ref.[50] over pressures of 2.0-3.5 GPa and temperatures of 400-900ºC, using the mineral-physics formulation by ref.[79] (Figs. 6a and S20). Pressure-temperature (P-T) trajectories along the oceanic Moho and 15 km below the oceanic Moho were extracted from the Ecuadorian slab thermal model[80] to calculate the corresponding Vs variations along the subducting slab (Fig. 6b). We additionally evaluated dry harzburgite along the slab-top P-T trajectory as a warm thermal reference to assess the maximum velocity reduction attributable to temperature under the modeled conditions (Fig. S20). The effective Vs of mixtures of dry and hydrated harzburgitic assemblages was calculated using Voigt-Reuss-Hill (VRH) averaging:

$$Vs_{vrh} = \sqrt{\frac{\theta \times G_{hyd} + (1-\theta) \times G_{dry}}{\theta \times \rho_{hyd} + (1-\theta) \times \rho_{dry}}}$$

where θ is the volume fraction of the hydrated endmember, and G and ρ are the shear modulus and density, respectively, of the hydrated and dry endmembers. The calculated velocities at representative P-T conditions corresponding to the mean depth of observed slab low velocity zone (SLVZ) were compared with the tomographic Vs value to estimate the range of hydrated-mineral abundances consistent with the observations (Fig. 6c). We also compared the SLVZ with the experimentally derived relationship between Vs and antigorite abundance reported by ref.[48].

We then investigated the potential contribution of partial melting to the mantle low-velocity zone within the overriding plate. The Vs of dry harzburgite was calculated over a similar pressure range of 2.0-3.5 GPa but at higher temperatures of 800-1500ºC (Fig. S21c). The corresponding dry and hydrous solidus conditions were evaluated following ref.[81]. We compared the calculated melt-free velocities along the solidi with the observed MLVZ velocities to assess whether temperature-dependent changes in the elastic properties of dry mantle rocks could account for the seismic observations (Fig. S21d). The effects of partial melting were further evaluated using the effective-medium model of ref.[54], considering different upper-mantle compositions (Fig 7d). The elastic properties of the solid host rocks and silicate melts required for the effective-medium calculations were determined using the dry harzburgitic mineral assemblage of ref.[50] and the major-element compositions of olivine-hosted melt inclusions in primitive mafic volcanic rocks from the Ecuadorian arc[82], respectively. The predicted effective Vs values were compared with the observed MLVZ velocities to estimate model-dependent melt fractions in the upper mantle of the overriding plate (Fig 7d).

Finally, we investigated the potential contribution of partial melting to the observed crustal low-velocity anomalies (CLVZ1 and CLVZ2) beneath the Ecuadorian volcanic arc. Given the compositional heterogeneity of the continental crust, we used Perple_X software to calculate equilibrium mineral assemblages based on the bulk-rock composition of the Ecuadorian Cordillera basement reported by ref.[83] (Table S1). The corresponding shear-wave velocities (Vs) were calculated over pressures of 0.4-1.6 GPa and temperatures of 500-1300ºC, along with the dry

solidus of the modeled crustal composition (Fig. S21a and S21b). We then modeled the relationship between Vs and melt fraction using the effective-medium models of ref. [53,54] (Fig 7b and 7c). The elastic properties of the solid crustal host rocks and silicate melts were calculated using the basement composition and the major-element compositions of volcanic rocks in the Ecuadorian arc[84-86] (Table S1), respectively. The predicted effective velocities were compared with the observed velocities to estimate model-dependent melt fractions (Fig 7b and 7c).

Data Availability

All the seismic data used in this study were requested from the NSF National Geophysical Facility data archive (https://service.earthscope.org/fdsnws/dataselect/1/) operated by EarthScope Consortium and from the Ecuador National Seismic Network[86] (REN-SIG). The seismic networks used in this study include the Ecuador RAMP Network[64] (8G), the High-Resolution Imaging of the Pedernales Earthquake Rupture Zone Broadband Network[66] (XF), the Ecuador Seismic Network[86] (EC), and Phase I and Phase II of the High-Resolution Imaging of the Pedernales Earthquake Rupture Zone nodal experiments[87,88] (XE; 2N).

Code Availability

The computer code for empirical Green's functions calculation is available in ref.[91]. The code for extraction of Rayleigh wave dispersion curve and phase velocity inversion is available in the CU-Boulder website (http://ciei.colorado.edu/Products/). The codes for Joint inversion of dispersion curves and receiver functions are available in a Zendo repository[92].

Author Contribution

Cong Li contributes to the conception, data curation and analysis, seismic imaging, formal analysis, result interpretations, and writing of the original paper. Susan L. Beck contributes to the conception, result interpretations, review and editing of the paper, and funding acquisition related to this study. Yi Wang contributes to the seismic imaging methodology, result interpretations and review and editing of the paper. Anne Meltzer contributes to the funding acquisition and review and editing of the paper. Colton Lynner and Mario Ruiz contributes to the data curation and review and editing of the paper.

Competing Interest

The authors declare no conflicts of interest relevant to this study.

Acknowledgements

This research was supported by the National Science Foundation grants EAR-1951203, EAR-2321410 and EAR-2321409. The temporary and broadband seismic instruments were provided by the EarthScope Consortium through the EarthScope Primary Instrument Center (IRIS PASSCAL at the time of the deployment) funded through the National Science Foundation's Seismological

Facility for the Advancement of Geoscience (SAGE). We thank staffs at Instituto Geofiísico at the Escuela Polite´cnica Nacional (IG-EPN) in Quito, Ecuador for their support and help.

References

1. Menard, H. W., & Atwater, T. (1969). Origin of fracture zone topography. *Nature, 222*(5197), 1037-1040.
2. Bach, W., Garrido, C. J., Paulick, H., Harvey, J., & Rosner, M. (2004). Seawater-peridotite interactions: First insights from ODP Leg 209, MAR 15˚N. *Geochem. Geophys. Geosyst., 5*(9). https://doi.org/10.1029/2004GC000744
3. Kil, Y., Lee, S. H., Park, M. H., & Wendlandt, R. F. (2010). Nature of serpentinization of ultramafic rocks from Hero Fracture Zone, Antarctic: Constraints from stable isotopes. *Mar. Geol., 274*(1–4), 43–49. https://doi.org/10.1016/j.margeo.2010.03.004
4. Kerrick, D. (2002). Serpentinite seduction. *Science. 298*, 1344-1345 https://doi.org/10.1126/science.298.5597.1344
5. Manea, V. C., Leeman, W. P., Zhu, G., & Martin, C. (2014). Subduction of fracture zones controls mantle melting and geochemical signature above slabs. *Nat. Commun., 5*(1), 5337. https://doi.org/10.1038/ncomms6095
6. Müller, R. D., Sdrolias, M., & Roest, W. R. (2012). The link between great earthquakes and the subduction of oceanic fracture zones. *Solid Earth, 3*(2), 447-453. https://doi.org/10.5194/se-3-447-2012
7. Ulmer, P., & Trommsdorff, V. (1995). Serpentine stability to mantle depths and subduction-related magmatism. *Science, 268* (5212), 858–861. https://doi.org/10.1126/science.268.5212.858
8. Burkett, E. R., & Billen, M. I. (2010). Three-dimensionality of slab detachment due to ridge-trench collision: Laterally simultaneous boudinage versus tear propagation. *Geochem. Geophys. Geosyst., 11*(11), Q11012. https://doi.org/10.1029/2010GC003286
9. Chen, Y., Gerya, T., & Liu, M. (2023). Vertical tearing of subducting plates controlled by geometry and rheology of oceanic plates. *Nat. Commun., 14*(1), 7904. https://doi.org/10.1038/s41467-023-43804-z
10. Hall, C. E., & Gurnis, M. (2005). Strength of fracture zones from their bathymetric and gravitational evolution. *Journal of Geophysical Research: Solid Earth*, 110(B1), B01402.
11. Hale, A. J., van Hunen, J., & Molnar, P. (2010). Dynamics of slab tear faults: Insights from numerical modelling. *Tectonophysics, 483*(1-2), 58-70. https://doi.org/10.1016/j.tecto.2009.05.019
12. Hey, R. (1977). Tectonic evolution of the Cocos-Nazca spreading center. *Geol. Soc. Am. Bull., 88*(12), 1404-1420. https://doi.org/10.1130/0016-7606(1977)88%3C1404:TEOTCS%3E2.0.CO;2
13. Harpp, K. S., Wanless, V. D., Otto, R. H., Hoernle, K., & Werner, R. (2005). The Cocos and Carnegie aseismic ridges: A trace element record of long-term plume-spreading center interaction. *J. Petrol., 46*(1), 109–133. https://doi.org/10.1093/petrology/egh064

14. Hardy, N. (1991). Tectonic evolution of the easternmost Panama basin: Some new data and inferences. *J. S. Am. Earth Sci., 4*(4), 261-269
15. Lonsdale, P. (2005). Creation of the Cocos and Nazca plates by fission of the Farallon plate. *Tectonophysics, 404*(1-4), 125-144. https://doi.org/10.1016/j.tecto.2005.05.011
16. Spikings, R., & Simpson, G. (2014). Rock uplift and exhumation of continental margins by the collision, accretion, and subduction of buoyant and topographically prominent oceanic crust. *Tectonics, 33*(5), 635–655. https://doi.org/10.1002/2013TC003425
17. Carena, S. (2011). Subducting-plate topography and nucleation of great and giant earthquakes along the South American trench. *Seismol. Res. Lett., 82*(5), 629–640.
18. Nocquet, J. M., Villegas-Lanza, J. C., Chlieh, M., Mothes, P. A., Rolandone, F., Jarrin, P., et al. (2014). Motion of continental slivers and creeping subduction in the northern Andes. *Nat. Geosci., 7*(4), 287–291. https://doi.org/10.1038/ngeo2099
19. Luzieux, L. D. A., Heller, F., Spikings, R., Vallejo, C. F., & Winkler, W. (2006). Origin and Cretaceous tectonic history of the coastal Ecuadorian forearc between 1°N and 3°S: Paleomagnetic, radiometric and fossil evidence. *Earth Planet. Sci. Lett., 249*(3–4), 400–414. https:// doi.org/10.1016/j.epsl.2006.07.008
20. Ancellin, M., Vlastélic, I., Samaniego, P., & Hidalgo, S. (2017). Across-arc versus along-arc Sr-Nd-Pb isotope variations in the Ecuadorian volcanic arc. *Geochem. Geophys. Geosyst., 18*(2), 551–575. https://doi.org/10.1002/2016GC006679
21. Bablon, M., Quidelleur, X., Samaniego, P., & Alvarado, A. (2019). Interactions between volcanism and geodynamics in the southern termination of the Ecuadorian arc. *Tectonophysics, 751*, 54-68. https://doi.org/10.1016/j.tecto.2018.12.010
22. Yepes, H., L. Audin, A. Alvarado, C. Beauval, J. Aguilar, Y. Font, and F. Cotton (2016), A new view for the geodynamics of Ecuador: Implication in seismogenic source definition and seismic hazard assessment. *Tectonics, 35*(5), 1249-1279, https://doi:10.1002/2015TC003941
23. Hayes, G. P., Moore, G. L., Portner, D. E., Hearne, M., Flamme, H. E., Furtney, M., & Smoczyk, G. M. (2018). Slab2, a comprehensive subduction zone geometry model. *Science, 362*(6410), 58–61. https://doi.org/10.1126/science.aat4723
24. Rosenbaum, G., Sandiford, M., Caulfield, J., & Garrison, J. M. (2019). A trapdoor mechanism for slab tearing and melt generation in the northern Andes. *Geology, 47*(1), 23–26. https://doi.org/10.1130/G45429.1
25. Hall, M. L., Samaniego, P., Le Pennec, J. L., & Johnson, J. B. (2008). Ecuadorian Andes volcanism: A review of Late Pliocene to present activity. *J. Volcanol. Geotherm. Res., 176*(1), 1-6. https://doi.org/10.1016/j.jvolgeores.2008.06.012
26. Ponce, G., Meltzer, A., Wickham-Piotrowski, A., Hoskins, M., Beck, S., Ruiz, M., et al. (2025). Insights into subduction zone complexity in the Northern Ecuadorian forearc from 3-D local earthquake tomography. *Geophys. J. Int., 242*(2), 189–208. https://doi.org/10.1093/gji/ggaf189

27. Rodríguez, E. E., Beck, S. L., Meltzer, A., Segovia, M., Ruíz, M., Hernández, S., et al. (2025). Seismic imaging of the Ecuadorian forearc and arc from joint ambient noise, local, and teleseismic tomography: Catching the Nazca slab in the act of flattening. *Geophys. J. Int., 241*(3), 1527–1553. https://doi.org/10.1093/gji/ggaf120
28. Vaca, S., Vallée, M., Nocquet, J. M., & Alvarado, A. (2019). Active deformation in Ecuador enlightened by a new waveform-based catalog of earthquake focal mechanisms. *J. S. Am. Earth Sci., 93*(449–461). https://doi.org/10.1016/J.JSAMES.2019.05.017
29. Wickham-Piotrowski, A. W., Meltzer, A. S., Ponce, G., Roecker, S., Beck, S. L., Ruíz, M., et al. (2025). High-density seismic network for improved tomographic imaging of the ecuadorian forearc: Slip mode controlled by in-situ material heterogeneity. *J. Geophys. Res.: Solid Earth, 130*(12), e2025JB031212. https://doi.org/10.1029/2025JB031212
30. Gutscher, M. A., Malavieille, J., Lallemand, S., & Collot, J. Y. (1999). Tectonic segmentation of the North Andean margin: Impact of the Carnegie Ridge collision. *Earth Planet. Sci. Lett.*, *168*(3–4), 255–270. https://doi.org/10.1016/S0012-821X(99)00060-6
31. Font, Y., Segovia, M., Vaca, S., & Theunissen, T. (2013). Seismicity patterns along the Ecuadorian subduction zone: New constraints from earthquake location in a 3D a priori velocity model. *Geophys. J. Int.,193*(1), 263–286. https://doi.org/10.1093/gji/ggs083
32. Collot, J. Y., Ratzov, G., Silva, P., Proust, J. N., Migeon, S., Hernández, M. J., et al. (2019). The Esmeraldas Canyon: A helpful marker of the Pliocene-Pleistocene tectonic deformation of the north Ecuador-Southwest Colombia convergent margin. *Tectonics, 38*(8), 3140–3166. https:// doi.org/10.1029/2019tc005501
33. Margirier, A., Strecker, M. R., Reiners, P. W., Thomson, S. N., Casado, I., George, S. W. M., & Alvarado, A. (2023). Late Miocene exhumation of the Western Cordillera, Ecuador, driven by increased coupling between the subducting Carnegie Ridge and the South American continent. *Tectonics, 42*(1), e2022TC007344. https://doi.org/10.1029/2022TC007344
34. Pedoja, K., Dumont, J. F., Lamothe, M., Ortlieb, L., Collot, J. Y., Ghaleb, B., et al. (2006). Plio-Quaternary uplift of the manta Peninsula and La Plata Island and the subduction of the Carnegie Ridge, central coast of Ecuador. *J. S. Am. Earth Sci., 22*(1–2), 1–21. https://doi.org/10.1016/j.jsames.2006.08.003
35. Li, C., Beck, S. L., Delph, J., Ericksen, B., Meltzer, A., Lynner, C., et al. (2026). High-resolution 3-D lithospheric structure of the subducting Carnegie Ridge and the Ecuadorian margin imaged from teleseismic receiver functions. *Geophys. Res. Lett., 53*, e2026GL122549. https://doi.org/10.1029/ 2026GL122549
36. Cahill, T., & Isacks, B. L. (1992). Seismicity and shape of the subducted Nazca Plate. *J. Geophys. Res. Solid Earth, 97*(B12), 17503-17529. https://doi.org/10.1029/92JB00493
37. Grove, T. L., Chatterjee, N. D., & Médard, E. (2006). The influence of H_2O on mantle wedge melting. *Earth Planet. Sci. Lett., 249*(1–2), 74–89. https://doi.org/10.1016/j.epsl.2006.06.043

38. Spandler, C., Pettke, T., & Hermann, J. (2014). Experimental study of trace element release during ultrahigh-pressure serpentinite dehydration. *Earth Planet. Sci. Lett., 391*, 296–306. https://doi.org/10.1016/J.EPSL.2014.02.010
39. Takeo, A., Kawakatsu, H., Isse, T., Nishida, K., Sugioka, H., Ito, A., & Shiobara, H. (2016). Seismic azimuthal anisotropy in the oceanic lithosphere and asthenosphere from broadband surface wave analysis of OBS array records at 60 Ma seafloor. *J. Geophys. Res. Solid Earth, 121*(3), 1927–1947. https://doi.org/10.1002/2015JB012429
40. Eilon, Z. C., & Forsyth, D. W. (2020). Depth-dependent azimuthal anisotropy beneath the Juan de Fuca plate system. *J. Geophys. Res. Solid Earth, 125*(6), e2020JB019477. https://doi.org/10.25349/D9N01T
41. Liu, C., Sheehan, A. F., & Ritzwoller, M. H. (2024). Seismic Azimuthal Anisotropy Beneath the Alaska Subduction Zone. *Geophys. Res. Lett., 51*(14), e2024GL109758. https://doi.org/10.1029/2024GL109758
42. Russell, J. B., Gaherty, J. B., Lin, P. Y. P., Lizarralde, D., Collins, J. A., Hirth, G. et al. (2019). High-Resolution Constraints on Pacific Upper Mantle Petrofabric Inferred From Surface-Wave Anisotropy. *J. Geophys. Res. Solid Earth, 124*(1), 631–657. https://doi.org/10.1029/2018JB016598
43. Yang, X., Luo, Y., Xu, H., & Zhao, K. (2020). Shear wave velocity and radial anisotropy structures beneath the central Pacific from surface wave analysis of OBS records. *Earth Planet. Sci. Lett., 534*, 116086. https://doi.org/10.1016/j.epsl.2020.116086
44. Miller, N. C., Lizarralde, D., Collins, J. A., Holbrook, W. S., & van Avendonk, H. J. A. (2020). Limited mantle hydration by bending faults at the Middle America Trench. *J. Geophys. Res. Solid Earth*, 125(12), e2020JB020982.
45. Ranero, C. R., Phipps Morgan, J., McIntosh, K., & Reichert, C. (2003). Bending-related faulting and mantle serpentinization at the Middle America trench. *Nature, 425*(6956), 367–373. https://doi.org/10.1038/nature01961
46. Van Avendonk, H. J. A., Holbrook, W. S., Lizarralde, D., & Denyer, P. (2011). Structure and serpentinization of the subducting Cocos plate offshore Nicaragua and Costa Rica. *Geochem. Geophys. Geosyst., 12*(6), Q06009. https://doi.org/10.1029/2011GC003592
47. Christensen, N. I. (2004). Serpentinites, peridotites, and seismology. *Int. Geol. Rev., 46*(9), 795–816. https://doi.org/10.2747/0020-6814.46.9.795
48. Ji, S., Li, A., Wang, Q., Long, C., Wang, H., Marcotte, D., et al. (2013). Seismic velocities, anisotropy, and shear-wave splitting of antigorite serpentinites and tectonic implications for subduction zones. *J. Geophys. Res. Solid Earth, 118*(3), 1015–1037. https://doi.org/10.1002/jgrb.50110
49. Ferrand, T. P., Hilairet, N., Incel, S., Deldicque, D., Labrousse, L., Gasc, J., et al. (2017). Dehydration-driven stress transfer triggers intermediate-depth earthquakes. *Nat. Commun., 8*(1), 15247. https://doi.org/10.1038/ncomms15247

50. Hacker, B. R., Abers, G. A., & Peacock, S. M. (2003). Subduction factory: 1. Theoretical mineralogy, densities, seismic wave speeds, and H_2O contents. *J. Geophys. Res. Solid Earth*, *108*(B1), 2029. https://doi.org/10.1029/2001JB001127
51. Jung, H., Green, H. W., II, & Dobrzhinetskaya, L. F. (2004). Intermediate-depth earthquake faulting by dehydration embrittlement with negative volume change. *Nature, 428*(6982), 545–549. https://doi.org/10.1038/nature02412
52. Rodríguez, E. E., Beck, S., Ruiz, M., Alvarado, P., Charvis, P., & Soto, H. (2023). Seismic imaging of the Northern Andean subduction zone from teleseismic tomography: a torn and fragmented Nazca slab. *Geophys. J. Int., 236*(1), 312–329. https://doi.org/10/1093/gji/ggad421
53. Chu, R., Helmberger, D. V., Sun, D., Jackson, J. M., & Zhu, L. (2010). Mushy magma beneath Yellowstone. *Geophys. Res. Lett., 37*(1), https://doi.org/10.1029/2009GL041656
54. Yoshino, T., Takei, Y., Wark, D. A., & Watson, E. B. (2005). Grain boundary wetness of texturally equilibrated rocks, with implications for seismic properties of the upper mantle. *J. Geophys. Res. Solid Earth, 110*. https://doi.org/10.1029/2004JB003544
55. Axen, G. J., van Wijk, J., & Currie, C. A. (2018). Basal continental mantle lithosphere displaced by flat-slab subduction. *Nat. Geosci., 11*(12), 961–964. https://doi.org/10.1038/s41561-018-0263-9
56. Grove, T. L., Till, C. B., & Krawczynski, M. J. (2012). The role of H_2O in subduction zone magmatism. *Annu. Rev. Earth Planet. Sci., 40*, 413–439. https://doi.org/10.1146/annurev-earth-042711-105310
57. Syracuse, E. M., van Keken, P. E., & Abers, G. A. (2010). The global range of subduction zone thermal models. *Phys. Earth Planet. Inter., 183*(1-2), 73-90. https://doi.org/10.1016/j.pepi.2010.02.004
58. Narváez, D. F., Samaniego, P., Koga, K. T., Rose-Koga, E. F., Hidalgo, S., & Ratzov, G. (2023). Two types of slab components under Ecuadorian volcanoes supported by primitive olivine-hosted melt inclusion study. *Lithos, 442–443*, 107049. https://doi.org/10.1016/j.lithos.2023.107049
59. Dzierma, Y., Thorwart, M., Rabbel, W., Siegmund, C., Comte, D., Bataille, K., Iglesia Llanos, M. P., & Prezzi, C. B. (2012a). Seismicity near the slip maximum of the 1960 Mw 9.5 Valdivia earthquake (Chile): Plate interface lock and reactivation of the subducted Valdivia Fracture Zone. *J. Geophys. Res. Solid Earth, 117*(B6), https://doi.org/10.1029/2011JB008914
60. Dzierma, Y., Rabbel, W., Thorwart, M., Koulakov, I., Wehrmann, H., Hoernle, K., & Comte, D. (2012b). Seismic velocity structure of the slab and continental plate in the region of the 1960 Valdivia (Chile) slip maximum — Insights into fluid release and plate coupling. *Earth Planet. Sci. Lett., 331–332*(18–31). https://doi.org/10.1016/j.epsl.2012.02.006
61. Ranero, C. R., Villaseñor, A., Morgan, J. P., & Weinrebe, W. (2005). Relationship between bend-faulting at trenches and intermediate-depth seismicity. *Geochem. Geophys. Geosyst., 6*(12), Q12002. https://doi.org/10.1029/2005GC000997

62. Bie, L., Hicks, S., Rietbrock, A., Goes, S., Collier, J., Rychert, C., et al. (2022). Imaging slab-transported fluids and their deep dehydration from seismic velocity tomography in the Lesser Antilles subduction zone. *Earth Planet. Sci. Lett., 586*, 117535. https://doi.org/10.1016/j.epsl.2022.117535
63. Sassard, V., Yang, X., Liu, L., & Elliott, J. L. (2025). Slab tearing along a subducted oceanic plate joint beneath the Alaska Peninsula. *Nat. Geosci., 18*(8), 801–807. https://doi.org/10.1038/s41561-025-01749-6
64. Ruíz, M. (2016). Ecuador RENSIG Data, Data Services Newsletter. (International Federation of Digital Seismograph Networks) data sets. https://www.fdsn.org/networks/detail/EC/.
65. Meltzer, A. & Beck, S. L. (2016) Pedernales Earthquake Aftershock Deployment Ecuador (International Federation of Digital Seismograph Networks) data sets. https://doi.org/10.7914/SN/8G_2016.
66. Regnier, M., Font, Y., Charvis, P., Mercerat, D., Rietbrock A., Ruiz M., et al. (2016). Pedernales [Data set]. International Federation of Digital Seismograph Networks. https://doi.org/10.7914/SN/XE_2016
67. Meltzer, A., Beck, S. L. & Stachnik., J. (2021) High Resolution Imaging of the Pedernales Earthquake Rupture Zone–Broadbands (International Federation of Digital Seismograph Networks) data sets. https://doi.org/10.7914/SN/XF_2021(2021).
68. Li, C., & Gao, H. (2021). Modification of crust and mantle lithosphere beneath the southern part of the eastern North American passive margin. *Geophys. Res. Lett.. 48*, e2020GL090555. https://doi.org/10.1029/2020GL090555.
69. Bensen, G. D. et al. Processing seismic ambient noise data to obtain reliable broad-band surface wave dispersion measurements. *Geophys. J. Int. 169*, 1239–1260. https://doi.org/10.1111/j.1365-246X.2007.03374.x (2007).
70. Lin, F. C., Ritzwoller, M. H., & Snieder, R. (2009). Eikonal tomography: Surface wave tomography by phase-front tracking across a regional broad-band seismic array. *Geophys. J. Int.*, 177(3), 1091–1110. https://doi.org/10.1111/j.1365-246X.2009.04105.x
71. Barmin, M. P., Ritzwoller, M. H., & Levshin, A. L. (2001). A fast and reliable method for surface wave tomography. *Pure Appl. Geophys., 158*(8), 1351-1375.
72. Lin, F. C., & Ritzwoller, M. H. (2011). Helmholtz surface wave tomography for isotropic and azimuthally anisotropic structure. *Geophys. J. Int., 186*(3), 1104–1120. https://doi.org/10.1111/j.1365-246X.2011.05070.x
73. Koch, C. D., Lynner, C., Delph, J., Beck, S. L., Meltzer, A., Font, Y., et al. (2020). Structure of the Ecuadorian forearc from the joint inversion of receiver functions and ambient noise surface waves. *Geophys. J. Int., 222*(3), 1671–1685. https://doi.org/10.1093/gji/gga a237
74. Koch, C. D., Delph, J., Beck, S. L., Lynner, C., Ruiz, M., Hernandez, S., et al. (2021). Crustal thickness and magma storage beneath the Ecuadorian arc. *J. S. Am. Earth Sci., 110*, 103331. https://doi.org/10.1016/j.jsames.2021.103331

75. Shen, W., Ritzwoller, M. H., Schulte-Pelkum, V., & Lin, F. (2013). Joint inversion of surface wave dispersion and receiver functions: A Bayesian Monte-Carlo approach. *Geophys. J. Int., 192*(2), 807–836. https://doi.org/10.1093/GJI%2FGGS050
76. Bodin, T., & Sambridge, M. (2009). Seismic tomography with the reversible jump algorithm. *Geophys. J. Int., 178*(3), 1411–1436. https://doi.org/10.1111/j.1365-246X.2009.04226.x
77. Bodin, T., Sambridge, M., Tkalčić, H., Arroucau, P., Gallagher, K., & Rawlinson, N. (2012). Transdimensional inversion of receiver functions and surface wave dispersion. *J. Geophys. Res.: Solid Earth, 117*(B2). https://doi.org/10.1029/2011JB008560
78. Álvarez-Gómez, J. A. (2019). FMC—Earthquake focal mechanisms data management, cluster and classification. *SoftwareX, 9*(299–307). https://doi.org/10.1016/j.softx.2019.03.008
79. Abers, G.A., & Hacker, B.R. (2016). A MATLAB toolbox and Excel workbook for calculating the densities, seismic wave speeds, and major element composition of minerals and rocks at pressure and temperature: *Geochem. Geophys. Geosyst., 17*(616–624), https://doi.org/10.1002/2015GC006171.
80. van Keken, P. E., & Wilson, C. R. (2023). An introductory review of the thermal structure of subduction zones: III—Comparison between models and observations. *Prog. Earth Planet. Sci., 10*(1), 57. https://doi.org/10.1186/s40645-023-00589-5
81. Katz, R. F., Spiegelman, M., & Langmuir, C. H. (2003). A new parameterization of hydrous mantle melting. *Geochem. Geophys. Geosyst., 4*(9), 1073. https://doi.org/10.1029/2002GC000433
82. Narváez, D. F.,, Rose-Koga, E. F., Samaniego, P., Koga, K. T., & Hidalgo, S. (2018). Constraining magma sources using primitive olivine-hosted melt inclusions from Puñalica and Sangay volcanoes (Ecuador). *Contrib. Mineral. Petrol., 173*(8), 65. https://doi.org/10.1007/s00410-018-1508-8
83. Hughes, R. A., & Pilatasig, L. F. (2002). Cretaceous and Tertiary terrane accretion in the Cordillera Occidental of the Andes of Ecuador. *Tectonophysics*, 345(1–4), 29–48. https://doi.org/10.1016/S0040-1951(01)00205-0
84. Samaniego, P., Robin, C., Chazot, G., Bourdon, E., & Cotten, J. (2010). Evolving metasomatic agent in the Northern Andean subduction zone, deduced from magma composition of the long-lived Pichincha volcanic complex (Ecuador). *Contrib. Mineral. Petrol., 160*(2), 239–260. https://doi.org/10.1007/s00410-009-0475-5
85. Samaniego, P., Le Pennec, J. L., Robin, C., & Hidalgo, S. (2011). Petrological analysis of the pre-eruptive magmatic process prior to the 2006 explosive eruptions at Tungurahua volcano (Ecuador). *J. Volcanol. Geotherm. Res., 199*(1-2), 69–84. https://doi.org/10.1016/j.jvolgeores.2010.10.010
86. Nauret, F., Samaniego, P., Ancellin, A., Tournigand, P., Le Pennec, J.-L., et al. (2018). The genetic relationship between andesites and dacites at Tungurahua volcano, Ecuador. *J. Volcanol. Geotherm. Res., 349*(283–297). https://dx.doi.org/10.1016/j.jvolgeores.2017.11.012

87. Meltzer, A., Beck, S. & Stachnik, J. (2020). High Resolution Imaging of the Pedernales Earthquake Rupture Zone - Nodes [Data set]. International Federation of Digital Seismograph Networks. https://doi.org/10.7914/SN/XE_2020
88. Meltzer, A., Beck, S. & Stachnik, J. (2022). High Resolution Imaging of the Pedernales Earthquake Rupture Zone - Nodes Phase II [Data set]. International Federation of Digital Seismograph Networks. https://doi.org/10.7914/SN/2N_2022
89. Global Volcanism Program, 2026. [Database] Volcanoes of the World. Distributed by Smithsonian Institution. https://doi.org/10.5479/si.GVP.VOTW5-2026.5.4
90. Frohlich, C., & Apperson, D. (1992). Earthquake focal mechanisms, moment tensors, and the consistency of seismic activity near plate boundaries. *Tectonics, 11*(2), 279–296. https://doi.org/10.1029/91TC02888
91. Chiaradia, M., Müntener, O., & Beate, B. (2020). Effects of aseismic ridge subduction on the geochemistry of frontal arc magmas. *Earth Planet. Sci. Lett.*, 531, 115984. https://doi.org/10.1016/j.epsl.2019.115984
92. Li. C. (2020). FullWaveformAmbientNoiseTomography: FWANT(v1.0.0) (Version v1.0) [Computer software]. Zenodo. https://doi.org/10.5281/zenodo.4021348
93. Li, C. (2026). TransBay_v1.0 [Computer software]. Zenodo. https://doi.org/10.5281/zenodo.24147469

Figures

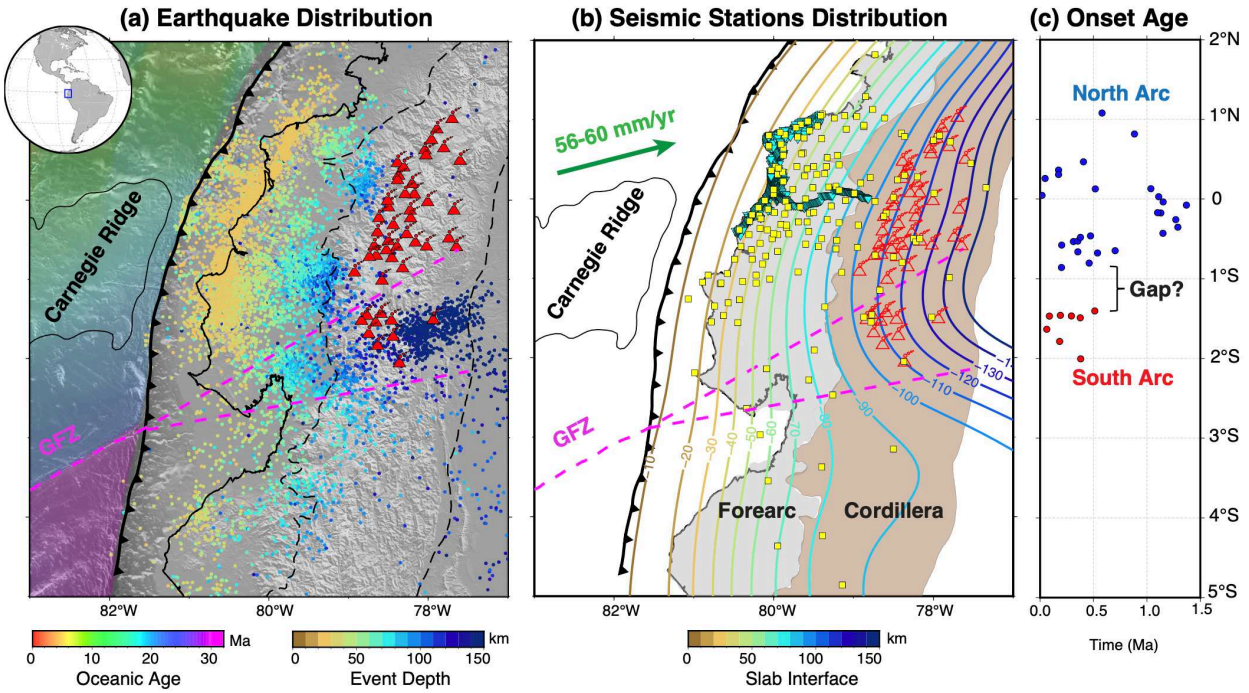


Figure 1. (a) Distribution of active volcanoes and subduction-zone earthquakes beneath Ecuador. Red cones denote Holocene and Pleistocene volcanoes along the Ecuadorian volcanic arc[89]. Colored circles show subduction-zone earthquakes from 2010-2022, identified by events located in the slab or no more than 5 km above the slab interface defined by ref.[30], or by the SLAB2 model[23] where the model of ref.[30] is unavailable. Earthquake locations are compiled from ref. [26,27,29]. The pink dashed line marks the projected inland continuation of the Grijalva Fracture Zone (GFZ)[22]. The black dashed line outlines the Ecuadorian Cordillera. The background shows offshore bathymetry overlain by the age of the incoming Nazca Plate and onshore topography. The thick and thin lines mark the trench and the Carnegie Ridge, respectively. (b) Map of the Ecuadorian forearc and arc and seismic stations used in this study. Yellow squares and inverted cyan triangles indicate broadband and nodal seismic stations, respectively. Green arrows show Nazca-South America convergence vectors[18]. Colored contours represent the slab interface from the Slab2 model[23]. (c) Along-strike variation in volcanic initiation age[21] along the Ecuadorian volcanic arc. Red and blue dot mark the volcanoes in the southern and northern arc, respectively.

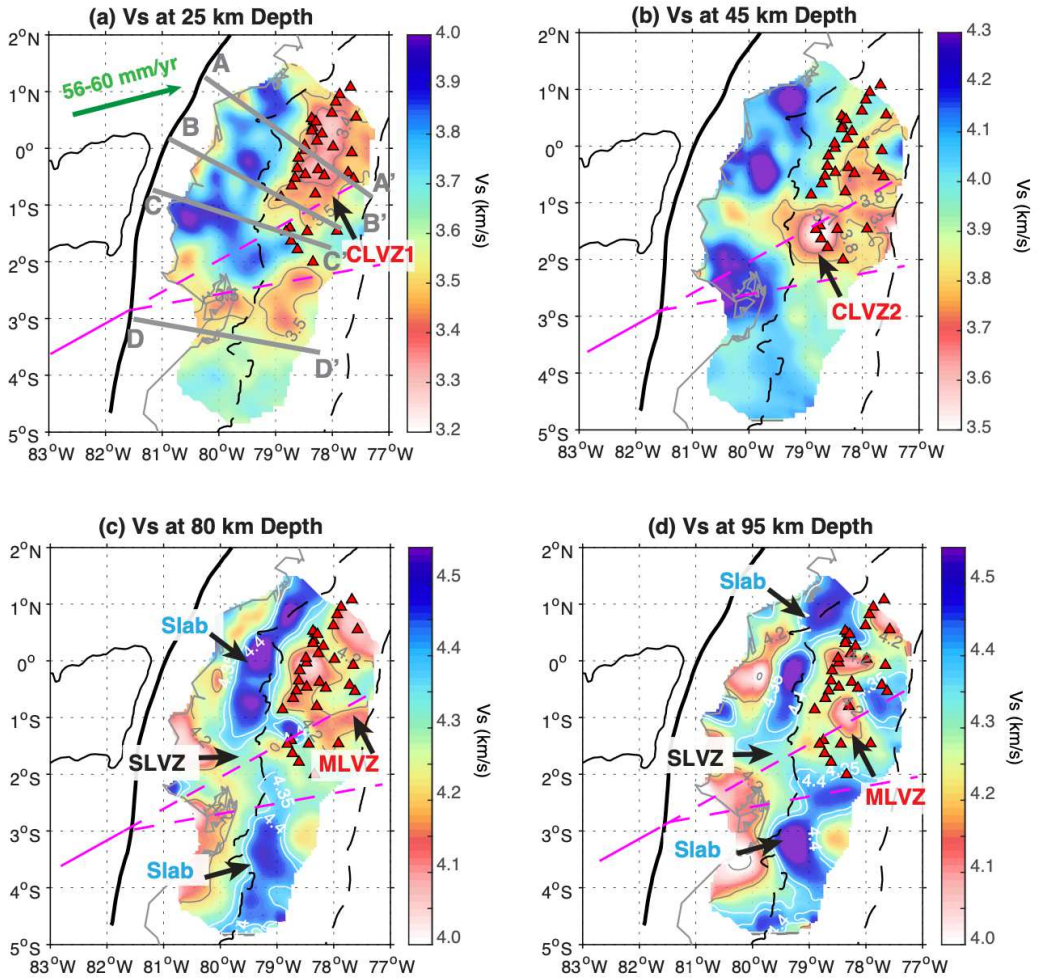


Figure 2. Shear-wave velocity (Vs) slices at multiple depths. The thick and thin black lines mark the trench and Carnegie Ridge, respectively. Onshore, black dashed lines mark the boundaries of the Cordilleras. Red triangles denote Holocene and Pleistocene volcanoes[89]. Pink dashed lines mark the inferred inland continuation of the Grijalva Fracture Zone (GFZ)[22]. Gray solid lines in (a) indicate the locations of the cross-sections shown in Figure 3. Note that the Vs color scale varies among depth slices to highlight velocity variations at different depths. Major velocity anomalies and their interpretations are labeled in each slice.

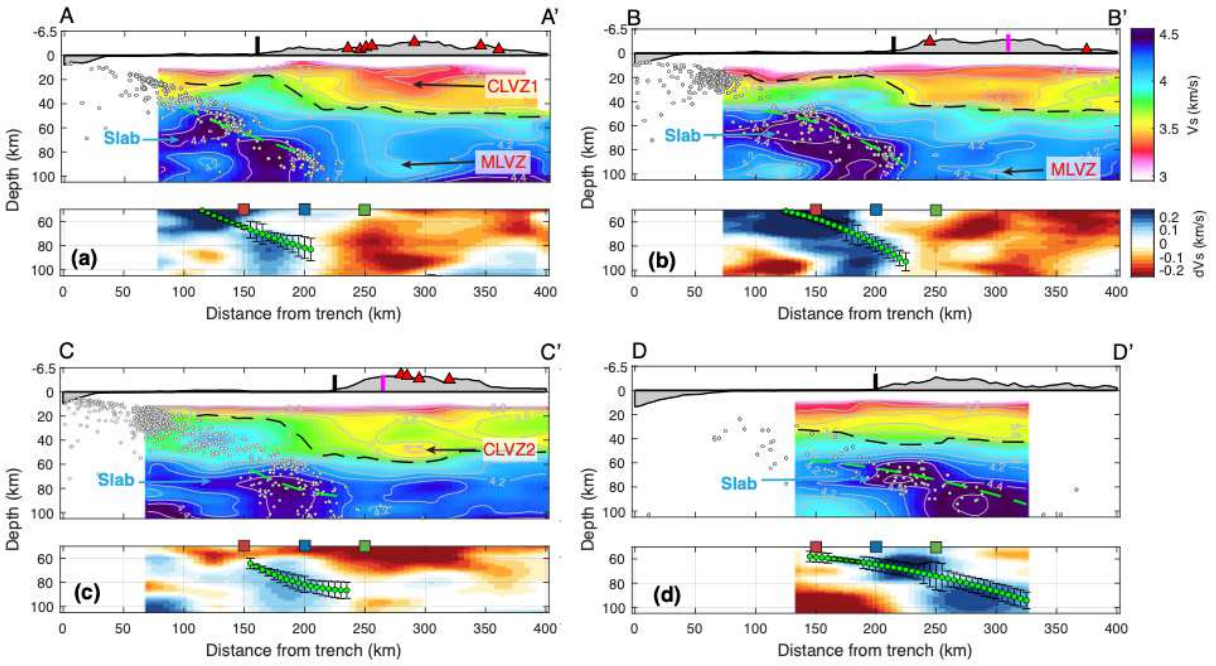


Figure 3. Cross-sections of the shear-wave velocity model (top) and velocity perturbation model (bottom). Cross-section locations are shown in Figure 2a. Black dashed lines mark sharp velocity discontinuities interpreted as the crust-mantle interface, whereas green dashed lines mark the inferred slab interface identified from the maximum positive vertical gradient in velocity perturbation. Topography is projected above each profile, with major geographic boundaries and the Grijalva Fracture Zone (GFZ) indicated by black and pink lines, respectively. Red triangles denote Holocene and Pleistocene volcanoes in the Ecuadorian Cordillera[89]. White dots represent subduction-zone earthquakes. Major velocity anomalies and their interpretations are labeled in each cross-section. In the lower panels, velocity perturbations at depths of 55-110 km are calculated relative to the mean Vs at each depth along the corresponding cross-section. Green dots with error bars indicate the locations of the maximum positive velocity-perturbation gradients used to constrain the inferred slab interface. Red, blue, and green squares mark distances of 150, 200, and 250 km from the trench, respectively. All cross-sections are plotted using the same Vs and velocity-perturbation scales.

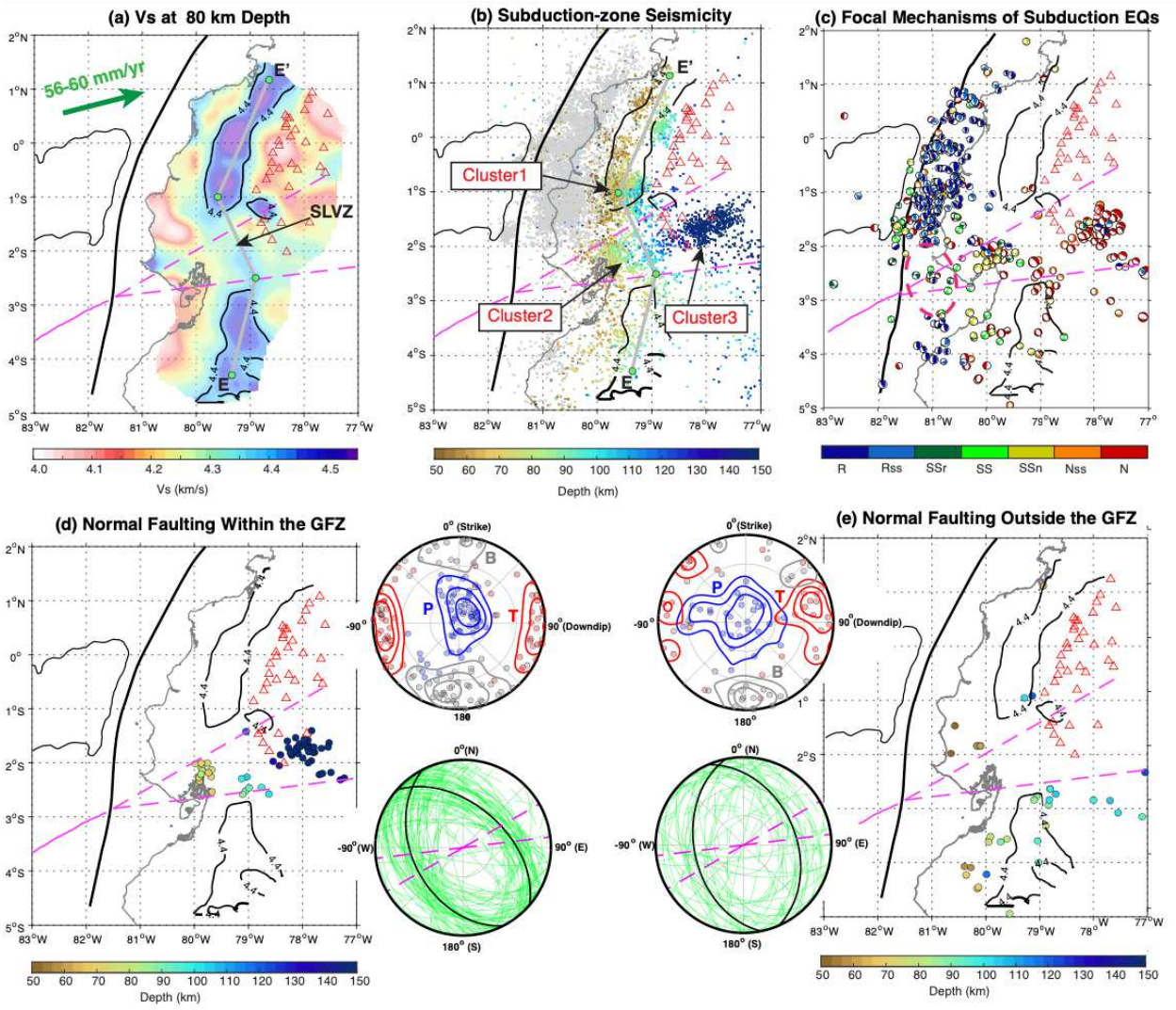


Figure 4. Comparison of shear-wave velocity structure, subduction-zone seismicity, and focal mechanisms. (a) Shear-wave velocity (Vs) slice at 80 km depth. The inferred slab is outlined by the 4.4 km/s Vs contour. The thick and thin black lines mark the trench and Carnegie Ridge, respectively. Red triangles denote Holocene and Pleistocene volcanoes[89]. The solid gray line marks the location of cross-section EE' shown in Figure 5, with the green dots indicating the kink points. Pink dashed lines mark the inferred boundaries of the inland continuation of the Grijalva Fracture Zone (GFZ)[22]. (b) Distribution of subduction-zone earthquakes beneath the Ecuadorian margin. Gray dots mark the events with depth shallower than 50 km, while the colored dots mark the events at greater depths. Other symbols are as in (a). (c) Focal mechanisms of subduction-zone earthquakes, colored according to the seven faulting classes[90]. (d) Distribution and focal mechanisms of subduction-zone earthquakes at depths larger than 50 km (i.e., intraslab earthquakes) within the inferred GFZ continuation zone. The stereonets at right show the distributions of P, T, and B axes in slab-relative coordinates (upper) and nodal planes geographic coordinates (lower). In the slab-relative reference frame, ±90° represents the slab downdip/updip

direction, 0° and 180° are parallel to the local slab strike, and the center of the stereonet represents the slab-normal direction. Blue, red, and gray dots and corresponding density contours represent the P, T, and B axes, respectively. Green great circles represent individual nodal planes, and the black great circle indicates their mean orientation. The nodal planes are rotated according to local slab dips. Pink dashed lines indicate the strike directions of the northern and southern boundaries of the inferred GFZ continuation. (e) Same as (d), but for intraslab earthquakes outside the inferred GFZ continuation zone.

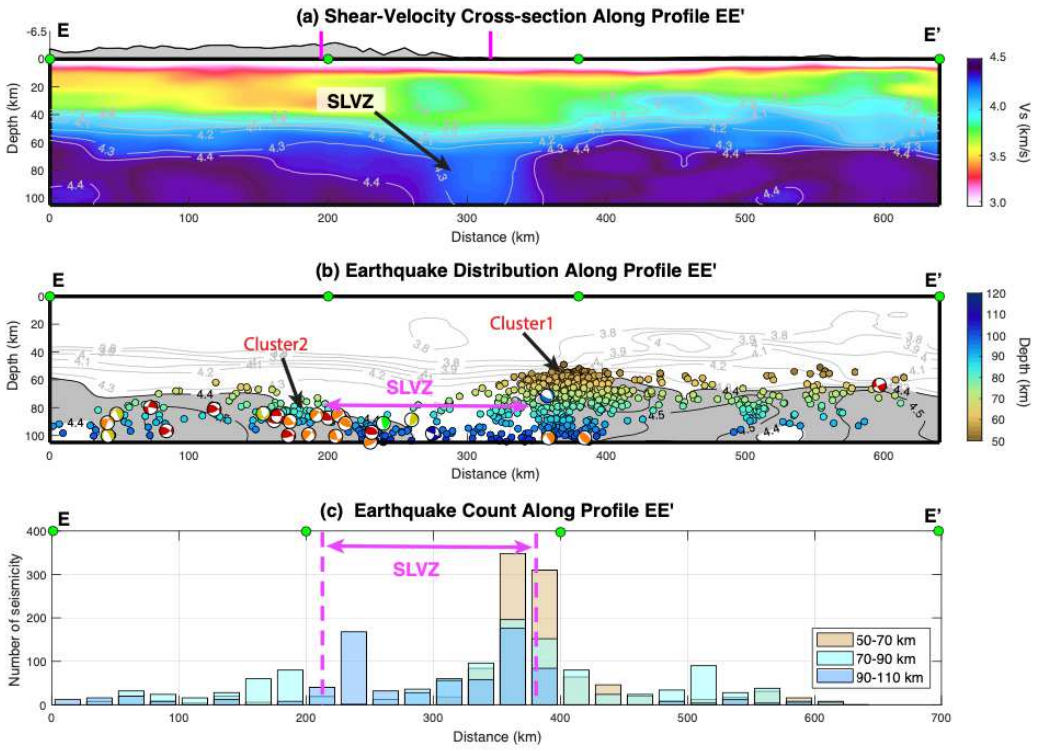


Figure 5. Comparison of shear-wave velocity structure and intraslab seismicity along cross-section EE'. (a) Shear-wave velocity (Vs) structure along EE'. The cross-section location is shown in Figure 4a. The depth-to-horizontal-distance aspect ratio is 1:1. The gray-filled area indicates topography, plotted with a vertical exaggeration of 3:1. Pink lines mark the northern and southern boundaries of the inferred inland continuation of the Grijalva Fracture Zone (GFZ). (b) Intraslab seismicity and focal mechanisms projected onto EE' using a projection width of 15 km on either side of the cross-section. Dots indicate earthquakes and are colored by hypocentral depth. Focal mechanisms are colored according to the seven faulting classes defined in Figure 4c. The two seismicity clusters identified in Figure 4b are indicated. The gray patches mark the subducting slab outlined by the 4.4 km/s Vs contour. The pink double-headed arrow marks the width of identified low-velocity zone in (a). (c) Earthquake counts along EE' for three depth intervals: 50-70, 70-90, and 90-110 km.

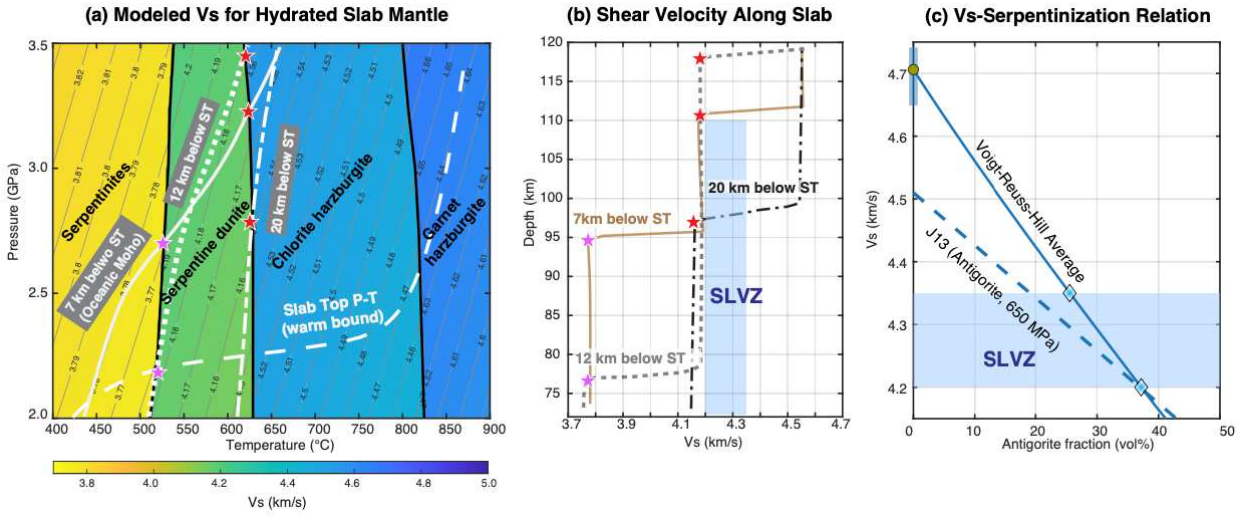


Figure 6. Petrophysical interpretation of the slab low-velocity zone (SLVZ). (a) Pressure-temperature-shear-wave velocity (P-T-Vs) diagram for hydrated harzburgitic slab mantle. Vs is calculated from the hydrated harzburgite mineral assemblages[50] and the mineral-physics formulation of ref.[79]. White solid, dashed, and dash-dotted lines show P-T trajectories along the slab top (ST), 7 km (approximate oceanic Moho), 12 km and 20 km below the slab top, respectively, from the thermal model for Ecuador[80]. The slab-top trajectory is shown as a warm thermal reference, whereas the Moho and sub-Moho trajectories represent conditions within the slab mantle. Thick black lines delineate mineral assemblage boundaries. Pink and red stars mark transitions from serpentinite to serpentine dunite and from serpentine dunite to chlorite harzburgite along the slab-mantle trajectory, reflecting progressive breakdown of antigorite. (b) Corresponding modeled Vs along P-T trajectories for the 7 km (brown dashed line), 12 km (gray dotted line) and 20 km below the slab top (black dash-dotted line). Pink and Red stars mark the mineralogical transitions identified in (a). The blue shaded region denotes the depth and Vs range of the SLVZ observed in Figures 4a and 5a. (c) Relationship between antigorite abundance and bulk Vs. The solid line shows Vs predicted by Voigt-Reuss-Hill averaging between dry and hydrated harzburgite endmembers, and the dashed line shows the experimental Vs-antigorite relationship[48] at 650 MPa. The blue shaded region denotes the Vs range in observed SLVZ. The blue bar at 0 vol. % antigorite fraction indicates the modeled Vs range of the dry-harzburgite endmember, and the olive circle marks the representative dry-harzburgite Vs at 2.5 GPa (~85 km depth) and 600 °C. Diamonds indicate the estimated antigorite abundances corresponding to the observed SLVZ velocities.

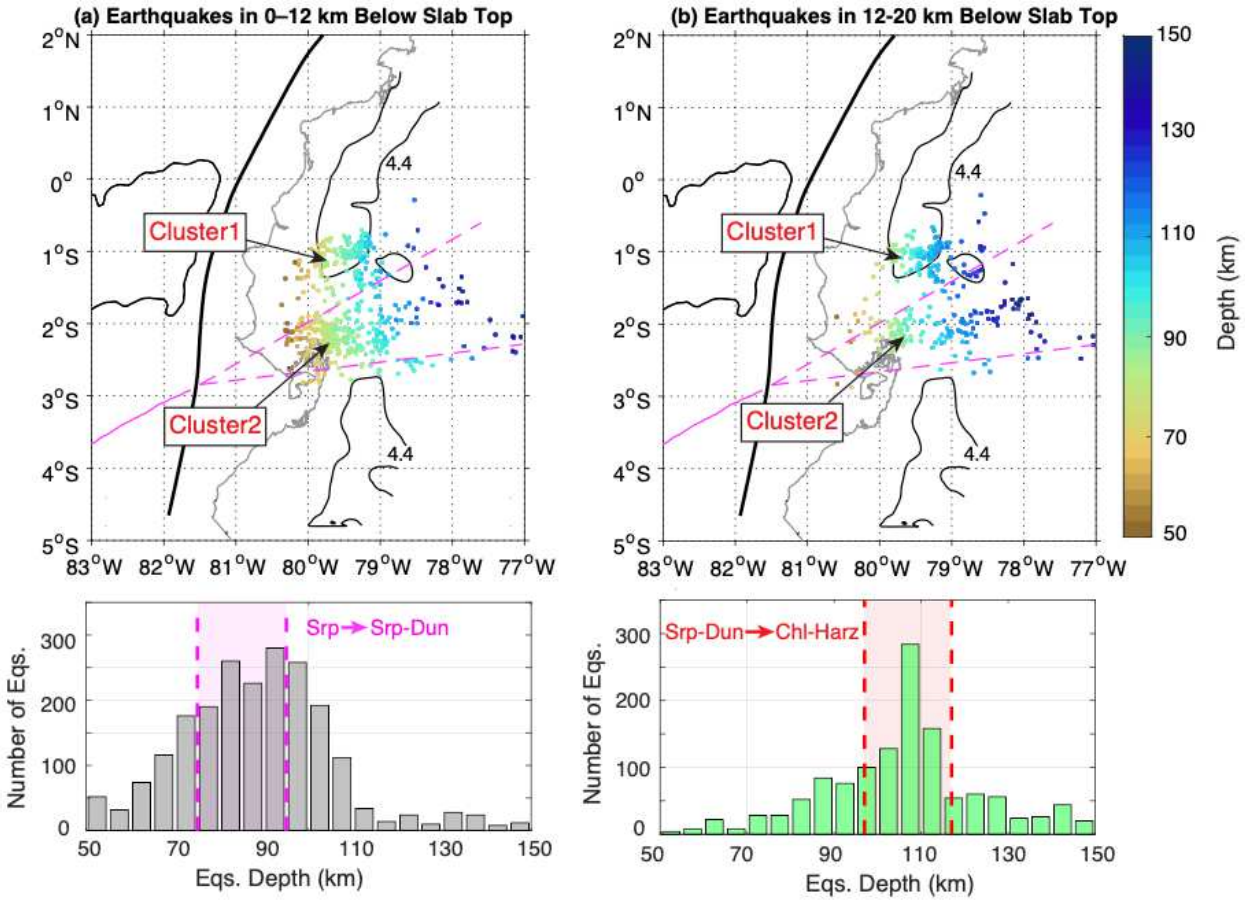


Figure 7. Depth distributions of intraslab earthquake clusters and their relationships to modeled mineralogical transitions. (a) Spatial (top) and depth (bottom) distributions of intraslab earthquake clusters located between the slab interface and 12 km below it. Dots in the upper panel indicate identified earthquake clusters near the imaged slab low-velocity column, colored by hypocentral depth. Other symbols are as in Fig. 4a. The lower panel shows the earthquake depth distribution in 5 km bins. The pink shaded region indicates the predicted depth range of the serpentinite-to-serpentine-dunite transition along the slab-mantle thermal trajectories shown in Fig. 6b. (b) Same as (a), but for intraslab earthquake clusters located 12-20 km below the slab interface. The red shaded region indicates the predicted depth range of the serpentine-dunite-to-chlorite-harzburgite transition shown in Fig. 6b.

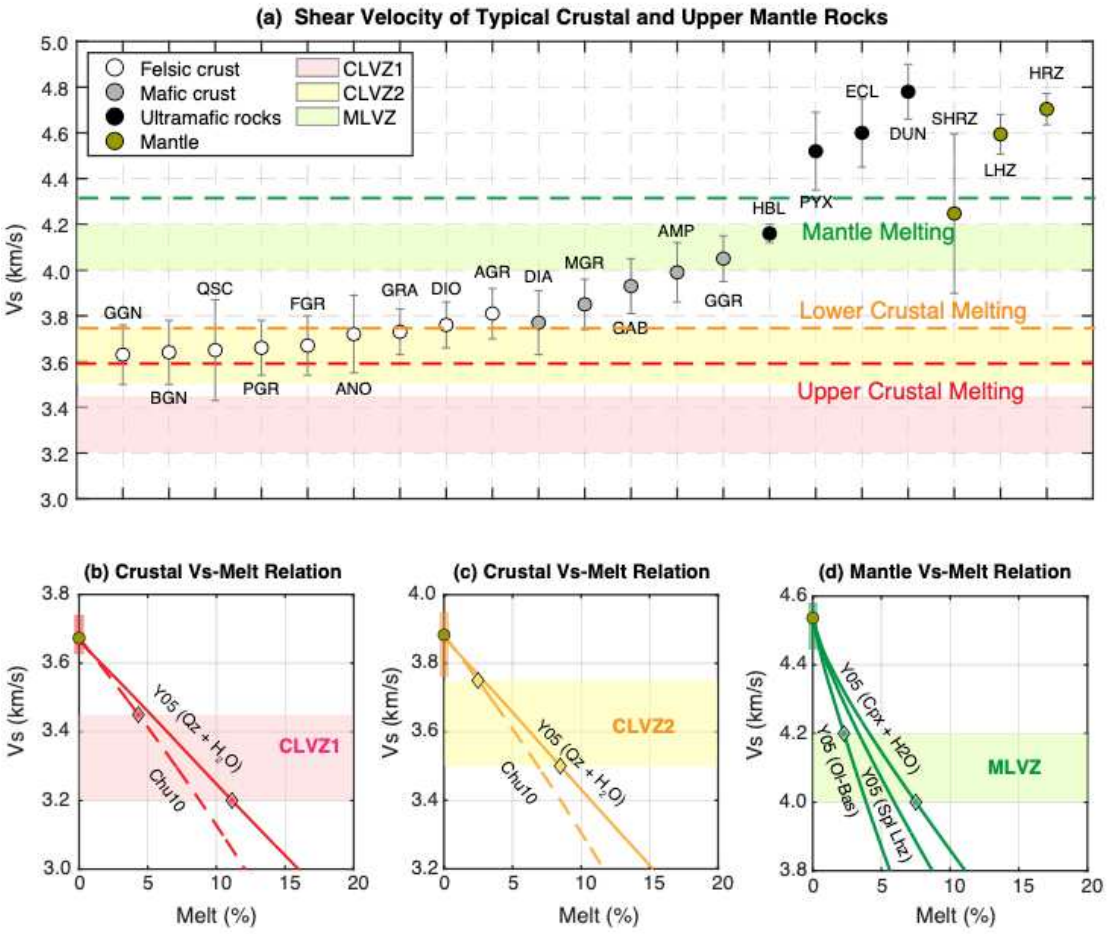


Figure 8. Petrophysical interpretation of subarc crustal and upper-mantle low-velocity zones. (a) Comparison of typical shear-wave velocities (Vs) of crustal and mantle rocks with the observed upper-to-middle crustal (CLVZ1; red shading), lower-crustal (CLVZ2; yellow shading), and upper-mantle (MLVZ; green shading) low-velocity zones. White, gray, and black circles indicate Vs of felsic, mafic, and ultramafic rocks, respectively, at 1 GPa from ref.[47]. Olive circles indicate representative mantle-rock velocities at 2.5-4 GPa and 600-1000 °C from ref.[50]. Red, orange, and green dashed lines indicate the minimum melt-free Vs along the dry solidus at the corresponding depth ranges of CLVZ1, CLVZ2, and MLVZ, respectively (Figure S25b and d). (b) Relationship between melt fraction and bulk Vs for CLVZ1. The red bar at 0% melt indicates the modeled Vs range of melt-free crustal rocks at 0.4-0.8 GPa along the dry solidus beneath the Ecuadorian volcanic arc. The olive circle indicates the melt-free reference Vs at 0.73 GPa (~25 km depth). Red solid and dashed curves show the effective-medium models Chu10[53]and Y05[54] and, respectively. Red shading denotes the observed Vs range of CLVZ1, and diamonds indicate the corresponding estimated melt fractions. (c) Same as (b), but for the lower-crustal anomaly CLVZ2. The orange bar at 0% melt indicates the modeled melt-free Vs range at 1.1-1.6 GPa along the dry solidus, and the olive circle indicates the reference Vs at 1.3 GPa (~45 km depth). Yellow shading denotes the observed Vs range of CLVZ2, and diamonds indicate the corresponding estimated melt fractions.

(d) Same as (b) and (c), but for the upper-mantle anomaly MLVZ. The green bar at 0% melt indicates the modeled Vs range of typical melt-free upper mantle rocks at 2.5-3.5 GPa along hydrous solidi. The olive circle indicates the reference Vs at 2.75 GPa (~85 km depth) along the 0.2 wt.% H_2O hydrous solidus. Green curves show the mantle effective-medium models (Y05). Green shading denotes the observed Vs range of MLVZ, and diamonds indicate the corresponding estimated melt fractions.

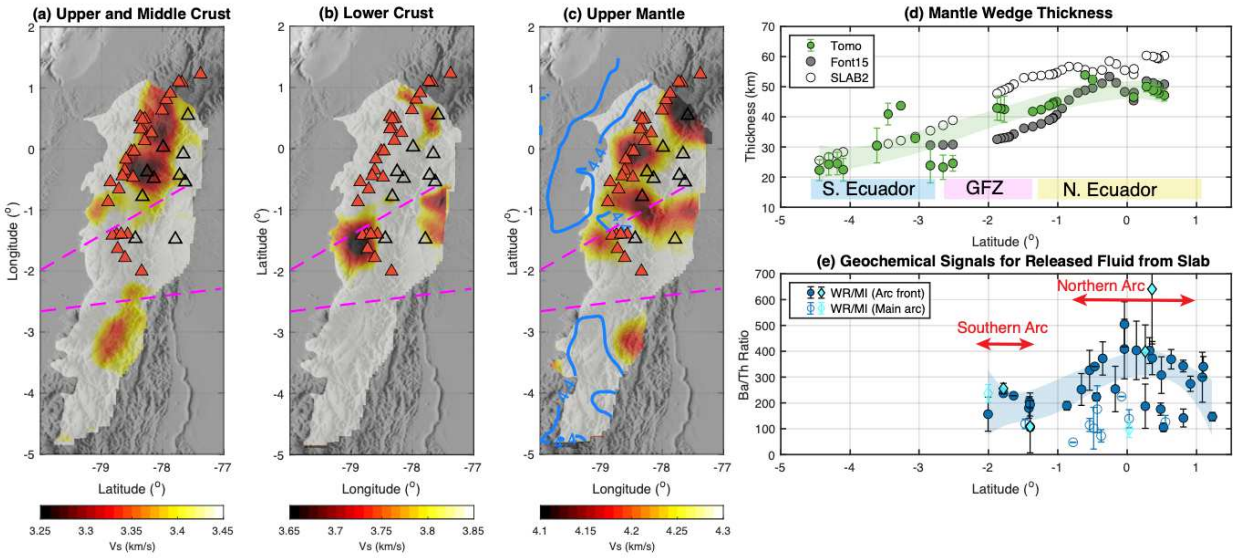


Figure 9. Comparison of subarc shear-wave velocity structure, mantle-wedge thickness, and geochemical signatures of slab-derived fluids. (a-c) Average shear-wave velocity (Vs) in the upper-to-middle crust, lower crust, and upper mantle, respectively, derived from the tomographic model. The crust and upper mantle are separated by the Moho, identified from the maximum positive vertical Vs gradient (Figs. 3 and S22). At each location, the crust is divided into equal upper-to-middle and lower crustal depth intervals based on the local Moho depth. Red filled triangles denote volcanoes along the volcanic front, whereas black open triangles denote volcanoes in the main arc and back arc. Pink dashed lines mark the inferred inland continuation zone of the Grijalva Fracture Zone (GFZ). (d) Mantle-wedge thickness, calculated as the vertical depth difference between the Moho and slab interface at a distance of 200 km from trench. Green circles show estimates based on the slab interface imaged in this study, whereas gray and open circles show estimates using the slab interfaces of ref.23 and 30, respectively. Colored bars indicate the southern Ecuador, GFZ, and northern Ecuador domains. (e) Latitudinal variation in Ba/Th ratios of volcanic rocks, used as a proxy for the contribution of slab-derived fluids to arc magmatism. Circles show whole-rock data from ref.[20,91], with filled and open symbols representing samples from the volcanic front and main/back arc, respectively. Diamonds show melt-inclusion data[58] that may more closely preserve primitive magma compositions.

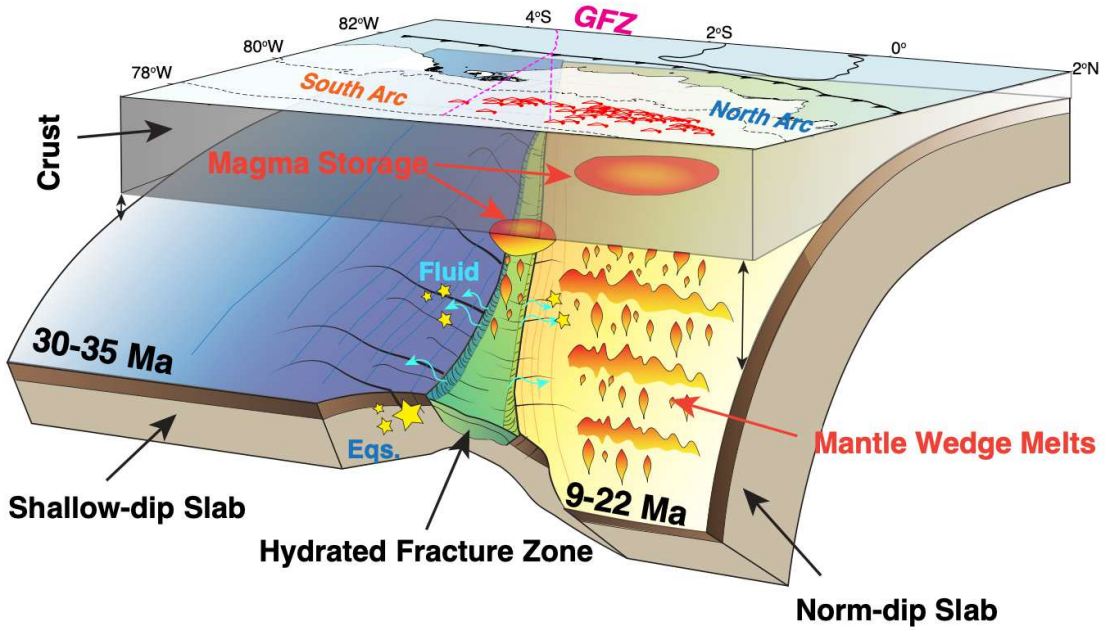


Figure 10. Schematic tectonic model illustrating the proposed influence of the Grijalva Fracture Zone (GFZ) on subduction dynamics beneath Ecuador. The GFZ represents an inherited lithospheric heterogeneity separating younger, moderately dipping Nazca lithosphere (~9-22 Ma) to the north from older, more gently dipping lithosphere (~30-35 Ma) to the south. The landward GFZ continuation forms a hydrated slab-mantle corridor between these contrasting slab segments, where progressive breakdown of hydrous minerals releases fluids that can promote localized intermediate-depth seismicity. Along-strike variations in slab geometry produce a thicker mantle wedge beneath northern Ecuador and a thinner wedge beneath southern Ecuador, favoring more extensive mantle melting in the north while limiting melt generation in the south. Additional fluids released from the hydrated GFZ corridor may locally enhance mantle melting and contribute to lower-crustal magma accumulation near its inferred inland continuation, but this effect is superimposed on broader variations in arc magmatism associated with slab geometry and thermal structure.

Supplementary Files

This is a list of supplementary files associated with this preprint. Click to download.

- SupplementaryInformationfinal.pdf